2011

In situ High-Pressure Studies of Hydrogen Storage Materials by Vibrational Spectroscopy

Ang Liu

Recommended Citation

Liu, Ang, "In situ High-Pressure Studies of Hydrogen Storage Materials by Vibrational Spectroscopy" (2011). *Digitized Theses*. 3402.
https://ir.lib.uwo.ca/digitizedtheses/3402

In situ High-Pressure Studies of Hydrogen Storage Materials by Vibrational Spectroscopy

(Spine Title: High Pressure Studies of Hydrogen Storage Materials)

(Thesis Format: Integrated-Article)

By

Ang Liu

Graduate Program in Chemistry

A thesis submitted in partial fulfillment
of the requirements for the degree of
Master of Science

The School of Graduate and Postdoctoral Studies
The University of Western Ontario
London, Ontario, Canada

THE UNIVERSITY OF WESTERN ONTARIO
SCHOOL OF GRADUATE AND POSTDOCTORAL STUDIES

CERTIFICATE OF EXAMINATION

Supervisor

Dr. Yang Song

Supervisory Committee

Examiners

Dr. Francois Lagugne-Labarthet

Dr. Styliani Constas

Dr. Jeffrey Hutter

The thesis by

Ang Liu

entitled:

In situ High-Pressure Studies of Hydrogen Storage Materials by Vibrational Spectroscopy

is accepted in partial fulfillment of the

requirements for the degree of

Master of Science

Date

Chair of the Thesis Examination Board

Abstract

Hydrogen has been considered as the most promising alternative source of energy as the world seeks a replacement for the conventional fossil fuel energy source. However, the storage of hydrogen still poses as a big challenge. As a result, development and investigation of hydrogen storage materials have received increasing attention. Here we report studies of two promising hydrogen storage materials, $NaNH_2$ and NH_3BH_3, under high pressure by Raman and IR spectroscopy.

First, sodium amide ($NaNH_2$) was investigated at room temperature and pressures up to 15 GPa. Starting with an orthorhombic crystal structure at ambient pressure, sodium amide was found to transform to two new phases upon compression as evidenced by changes of characteristic Raman and IR modes as well as by examining the pressure dependences of these modes. Raman and IR measurements on $NaNH_2$ collectively provided consistent information about the structural evolution of $NaNH_2$ under compression. Upon decompression, all Raman and IR modes were completely recovered indicating the reversibility of the pressure-induced transformations in the entire pressure region. The Raman and IR spectroscopic data together allowed for the analysis of possible structures of the new high-pressure phases of $NaNH_2$.

Another potential hydrogen storage material, ammonia borane (NH_3BH_3), was investigated at simultaneous high pressures (up to 15 GPa) in a diamond anvil cell and low temperatures (down to 80 K) using a cryostat by Raman spectroscopy *in situ*. Upon cooling from room temperature to 220 K at near ambient pressure, an expected phase transformation from $I4mm$ to $Pmn2_1$ was observed. Then the sample was compressed to

15 GPa isothermally at 180 K. Three pressure induced structural transformations were observed as evidenced by the change of Raman profile as well as the pressure dependence of the major Raman modes. The decompression and warming-up experiments suggest these P-T-induced transformations are reversible. These observations, together with factor group analysis, allowed us to examine the possible structures of the new high pressure phases and the nature of phase transitions. Raman measurements from multiple runs covering various P-T paths, when combined with previously established room-temperature and high-pressure data, enabled the update of the P-T phase diagram of ammonia borane in the pressure region of 0-15 GPa and the temperature region of 80-350 K.

Keywords

High pressure · Low temperature · Hydrogen storage materials · Raman and IR spectroscopy · Diamond anvil cell · Sodium amide · Ammonia borane · Phase transitions

The Co-Authorship Statement

I hereby declare that this thesis consists of independent research, and the work in both papers of which I am the first author who made a major contribution to the work in the research and writing phase will form part of the Master of Science thesis. In both cases, experimental designs, data analysis and interpretation, and the initial draft writing were performed by me. My advisor, Dr. Yang Song, helped me solve some of problems in the experiments and data analysis as well as manuscript revisions.

I am aware of the University of Western Ontario Policy on Authorship and I certify that I have properly acknowledged the contribution of other researchers to my thesis.

I certify that, with the above qualifications, this thesis, and the research to which it refers, is the product of my own work.

Acknowledgements

First and foremost, I would like to acknowledge my great advisor Prof. Yang Song for his supervision and guidance during the past two years in the exciting field of "high pressure studies of hydrogen storage materials". His continuous guidance enabled me to complete my work successfully. I have furthermore to thank Dr. Nicholas C. Payne and Dr. Lyudmila Goncharova, for their teaching and help in and outside their courses.

I would also like to thank all the members of the Song group, especially Ms. Zhaohui Dong, who helped me a lot in every aspect of my life including studies, lab assistance and life. I would like to say to her: "Although we are not blood-related, but to me you are my real sister forever, ever!" Also, many thanks to Dr. Kirill Zhuravlev for helping me with the low-temperature measurements.

Additionally, I wish to thank the TA laboratory technicians, Sandy (Sandra Zakaria Holtslag) and Jane for their help and support in the last two years. The time I spent with the smart and beautiful canadian undergraduates, Sandy, Jane and other TAs leaves great happy memory in my life. I am also grateful for the recommendation letter from Sandy.

Special thanks to my friends (Jing Chao and her husband Qing Mu, Lijia Liu, Jun Xu, Michael Linda Wu, Shuntai Xie, Jia Jia, Donghan Chen, Jiacheng Guo, Yue Hu, Zhu Lin, Yunying Shen, Radu, Amanda, Racheal and Jing Zhang) and classmates (Sarah, Xiangrong Zhang and Zhao). It is you who drive the loneliness away from me and leave a happy and memorable time to me.

I thank the help from Darlene McDonald, Clara Fernandes and the guys in the machine shop (Barakat, John and Jon).

Finally I would like to thank my parents for their love, understanding and support during my M.Sc. studies and in my decisions of future developments.

Table of Contents

List of Figures

List of Tables

List of Abbreviations

asym.	asymmetric
CCD	charge-coupled device
DAC	diamond anvil cell
Fig.	figure
GPa	gigapascal
INS	inelastic neutron scattering
IR	Infrared
MPa	megapascal
Mrad	milliradian
sym.	symmetric
THF	tetrahydrofuran
XRD	X-ray diffraction

Chapter 1 Introduction

1.1 Hydrogen and hydrogen storage

1.1.1 Hydrogen

Fossil fuels have been used as the primary energy source for centuries in the modern world, resulting in serious environmental pollution and undesired hazardous consequences, e.g., the global warming which leads to increasing sea level and the expansion of infectious diseases. Therefore alternative energy sources, such as solar energy, wind energy, geothermal energy, bioenergy and hydrogen energy, are needed to meet the needs of contemporary society and protect the environment because they generally have high energy efficiency and leave little environmental traces. [1,2]

Once manufactured from natural chemicals, pure hydrogen becomes an energy carrier and the most promising energy source due to its high efficiency, little emissions of carbon dioxide (lifecycle CO_2 emissions per km would be less than 1/5 of those for gasoline combustion) and high heating value per mass compared to other chemical fuels. All these outstanding properties make it the most suitable candidate for both the portable and stationary applications. Recently, by combining the proper catalysts and the membrane, scientists have developed new fuel cells based on the combustion of high purity hydrogen with only one product, water. [2-5]

1.1.2 Hydrogen storage

A world-scale environmentally cleaner hydrogen economy is growing faster nowadays, but the production, storage and delivery of hydrogen are still the major concerns towards its commercialization.[4,6] Especially about the hydrogen storage issues, the US Department of Energy (DOE) has set the ambitious target, i.e., by 2015, a gravimetric density of 9.0 wt% H and a volumetric density of 82 $g\text{-}H_2 \cdot L^{-1}$ should be achieved.[6-7] As a result, extensive research effort has been put into the development of effective hydrogen storage strategies.

In general, hydrogen storage can be divided into two categories: physical storage and chemical storage. Each category involves confinement of hydrogen in different states, such as a compressed gas, liquid, absorbed on materials and chemically bonded in covalent and ionic compounds.[8] On one hand, physical storage carries large weight of hydrogen in the hydrogen storage system, such as in the cryo-compressed storage of hydrogen, porous metal-organic frameworks, clathrate hydrates and carbon nanotubes. It was reported that nanostructured carbon (e.g., buckyballs and nanotubes) can adsorb a large amount of hydrogen (hydrogen storage capacity ranges from 0.2 to 10 wt%) because of their effective porosity and carbon structures.[9] For the chemical storage, on the other hand, hydrogen can be stored in solid state chemical materials[10] which include carbon-based chemicals,[9,11-16] metal hydrides,[17-21] chemical hydrides[22-26] and complex hydrides.[5,18,22,27-29] It was also found that metal hydrides, e.g., $NaAlH_4$,[30] $LiAlH_4$,[31-32] MgH_2,[33-34] $LiNH_2$,[33,35-36] can be used as storage medium for hydrogen due to their strong binding interactions with hydrogen molecules. Among them, sodium, lithium and boron based compounds become leading candidates for storage applications due to their high hydrogen gravimetric percentage. Distinct from metal hydrides, chemical hydrides generally require a chemical reaction pathway to be regenerated. As a result, the refueling of the vehicle could not be achieved directly.[18,37-39]

More recently, the high pressure technique has demonstrated strong promises as an alternative approach to develop hydrogen storage materials. Therefore, in the next several sections, we will discuss the principles of the high pressure technique and its implications on the development of novel potential hydrogen storage materials.

1.2 High pressure science and technology

1.2.1 High pressure phenomena

To describe a thermodynamic system, three macroscopic variables (temperature, pressure and volume) are used. Among these parameters, pressure spans over 60 orders of magnitude in the universe, i.e., from 10^{-32} Pascal in intergalactic space to 10^{32} Pascal in the center of neutron star. In the laboratory, the accessible pressure region was advanced by several orders of magnitudes (400 MPa to 40,000 MPa) by Percy Williams Bridgman. More recently, static pressures at the 100 GPa scale (1 GPa=10^3 MPa=10^9 Pa≈10^4 atm), close to the pressure in the earth core (around 330-360 GPa), have been generated in some laboratories.[40-41]

Recent high pressure experiments have revealed interesting phenomena and produced novel materials with exotic structures and properties.[42] Under the high pressures the interatomic distance and thus the nature of intermolecular interactions, chemical bonding, molecular configuration, crystal structure, and stability of solids could be significantly altered.[43-44] Firstly, high pressure conditions will lead to a change of intra- or inter- molecular interactions and thus the stabilities of materials. Advanced high pressure experiments have demonstrated the formation of novel materials, such as superhard materials[45-47] and superconductors.[48-50] For example, the high pressure form of graphite is superhard, capable of identing diamond single crystals.[45] As another example, by magnetic susceptibility and electrical resistivity measurements, superconductivity of condensed phases of lithium were observed.[50] More importantly, high pressures serve as an important tool to tune the electronic, magnetic, optical and mechanical properties for testing theories and expanding applications.[51]

1.2.2 Diamond anvil cell

Scientists expedited the process of high pressure studies in the last few decades by employing a new kind of device called the diamond anvil cell (DAC), which was used to generate high pressures up to ~ 360 GPa. The predecessor of the modern DAC with two opposing anvils was invented by Percy Williams Bridgman who was awarded the Nobel Prize in physics (1946). He developed an opposed anvil device made of tungsten-carbon alloy (WC) with small flat areas that were pressed against each other with a lever-arm. Pressures of a few GPa could be achieved by this device which was used in electrical resistance and compressibility measurements. Based on this configuration, the modern DAC in which the diamonds were used as anvils was developed by Weir and his colleagues in the National Bureau of Standards.[52-53] Diamonds are known as the hardest material in nature and are therefore suitable for high pressure generation. Additionally, diamonds are transparent to a wide spectral range of electromagnetic radiation, and thus can be utilized in the structural characterization of materials under high pressure by various probes, such as vibrational spectroscopy and X-ray diffraction (XRD). Type I diamonds which have higher impurity (e.g. nitrogen) are used for Raman and XRD measurements, while type II diamonds are employed in infrared (IR) measurements.

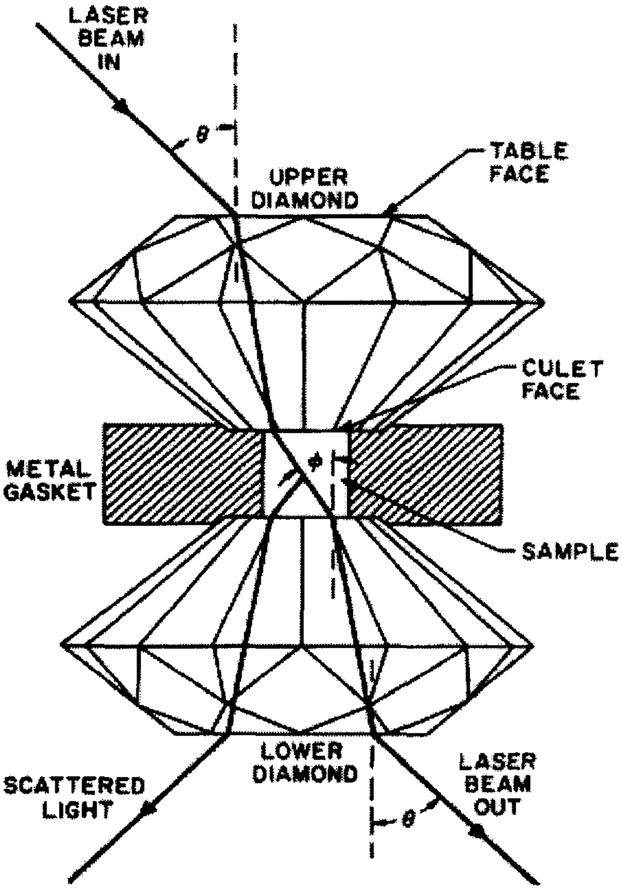

Fig. 1.1 General schematic of a symmetric diamond anvil cell. (Adapted from Ref. 54)

The schematic of a symmetric DAC is shown in Fig. 1.1. A pair of identical diamond anvils is placed between the two supporting seats, typically made of tungsten carbide, which accommodate the tightening screws. A pre-indented gasket with a hole drilled in the center serves as the sample chamber, and is placed between the two diamonds. Once a small force is applied to the DAC, the backup seats will generate a pressure that is amplified by the shape of the diamond, yielding a high pressure on the diamond tip and an even higher pressure in the gasket and sample. The pressure can be calibrated by the ruby gauge described below.

To meet the various requirements for experiments in different physical conditions, customized DACs are designed and made, such as symmetric DAC for room-temperature measurements,[54-55] specially designed Be-Cu DACs to be fit into a cryostat for low-temperature measurements[56] and the Merrill-Bassett type DAC for high pressure/high temperature experiments.[57]

1.2.3 The ruby pressure gauge

For all high pressure experiments, it is extremely important to precisely and accurately determine the pressure inside the DAC. Mao has reported the equation shown below for determining the pressure with an accuracy of ± 0.05 GPa by measuring ruby (α-Al_2O_3 doped with Cr^{3+}) fluorescence spectra.[58]

$$P = \frac{1904}{B}[(1+\frac{\Delta\lambda}{694.24})^B - 1] \qquad (1.1)$$

where P is the pressure in GPa and $\Delta\lambda$ is the difference between the wavelength of the ruby R_1 line at pressure P and that at ambient pressure. For example, the difference between the wavelengths of Ruby R_1 fluorescence spectra at 8.3 GPa and at 17.8 GPa was used to determine the higher pressure. (Fig 1.2) The parameter B is equal to 7.665 for quasi-hydrostatic conditions, and is 5 for non-hydrostatic conditions.[58]

Holzapfel and coworkers developed two empirical approximations for the temperature dependence of the ruby R_1 line for calibration at temperature T relative to a reference temperature T_0.[59] The more complex approximation, used over a wider range of temperatures, is

$$\nu_0(T) = \nu_0(T_0) - 3.551\times10^{-8}[\ln(T/T_0)]^{11.54} \qquad (1.2)$$

where $\nu_0(T)$ and $\nu_0(T_0)$ are the frequencies (in cm^{-1}) of maximum intensity of the R_1 line at ambient pressure and temperatures T and T_0, respectively.[59]

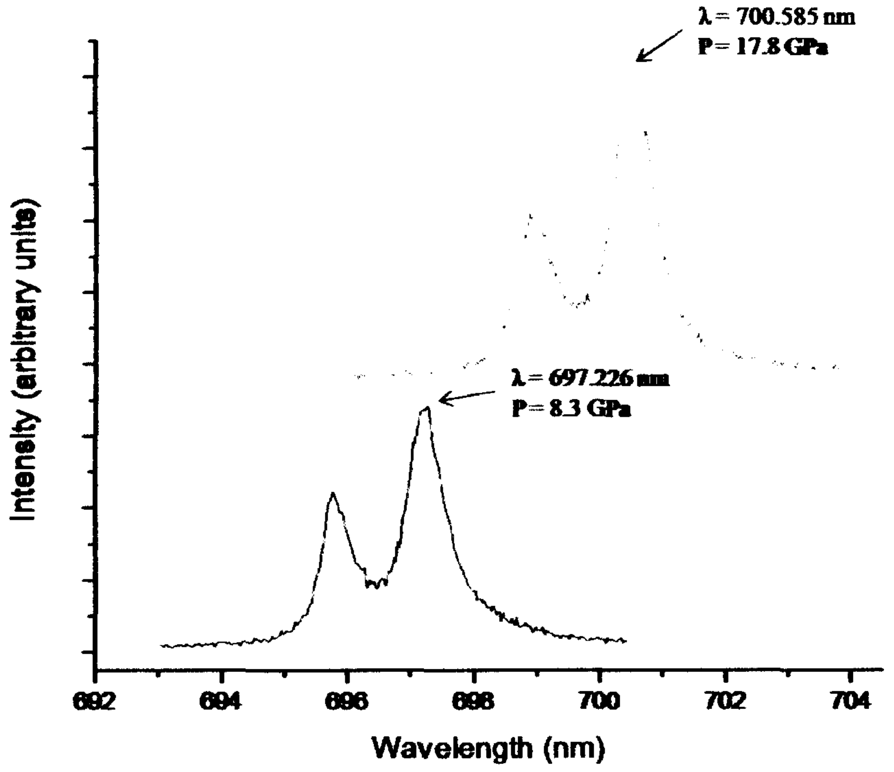

Fig. 1.2 Ruby R_1 fluorescence spectra at 8.3 GPa (in black) and at 17.8 GPa (in red) at room temperature.

1.2.4 High-pressure vibrational spectroscopy

In our studies, two commonly used spectroscopies for characterizing the vibrations of different materials under high pressures are Raman and IR absorption spectroscopies. Both of them are based on molecular vibrations, but each has its own focuses, e.g., Raman is based on polarisability of the molecule and therefore reveals a series of vibrational modes in the lattice region, while IR is based on the molecular dipole moment and therefore reflects the bending and stretching characteristics. IR spectra are complementary to Raman spectra and may provide more information on molecular symmetry while Raman gives substantial structural information.

Raman spectroscopy is based on the scattering of monochromatic light, usually from a laser in the visible, near infrared, or near ultraviolet range. A small fraction of laser photons are scattered after inelastic interactions with atoms or molecules in the sample while most of the scattered photons, which is referred to as Rayleigh scattering, have the same frequency as the incident beam and therefore carry no spectroscopic information. Meanwhile, some photons are scattered with frequencies higher or lower than the incident beam; the former process is referred to as anti-Stokes scattering while the latter is called Stokes scattering. Energies between Stokes or anti-Stokes and the incident beams fall into the gaps between different vibrational or rotational energy levels of the molecule in the sample. Thus, the measurement of Raman shifts (energy differences between Stokes/anti-Stokes and the incident beam) provides valuable spectroscopic information for the vibrational or rotational energy levels of that sample.[40]

A customized Raman micro-spectroscopy system in our lab was used to collect the Raman spectra. Fig. 1.3 shows a photo of the system. Briefly, an Innova Ar^+ laser (Coherent Inc.) was used as the excitation source. The laser was focused to the sample by Mitutoyo objective. The Raman signal was detected with backscattering geometry by the same objective lens. The Rayleigh scattering was removed by a pair of notch filters. The scattered light was then dispersed using an imaging spectrograph equipped with several gratings. The Raman signal was recorded using an ultrasensitive, liquid nitrogen cooled, back-illuminated, charge-coupled device (CCD) detector from Acton. The system was calibrated by neon lines. More detailed experimental parameters were set according to the individual experiments as outlined in Chapters 2 and 3.[60-61]

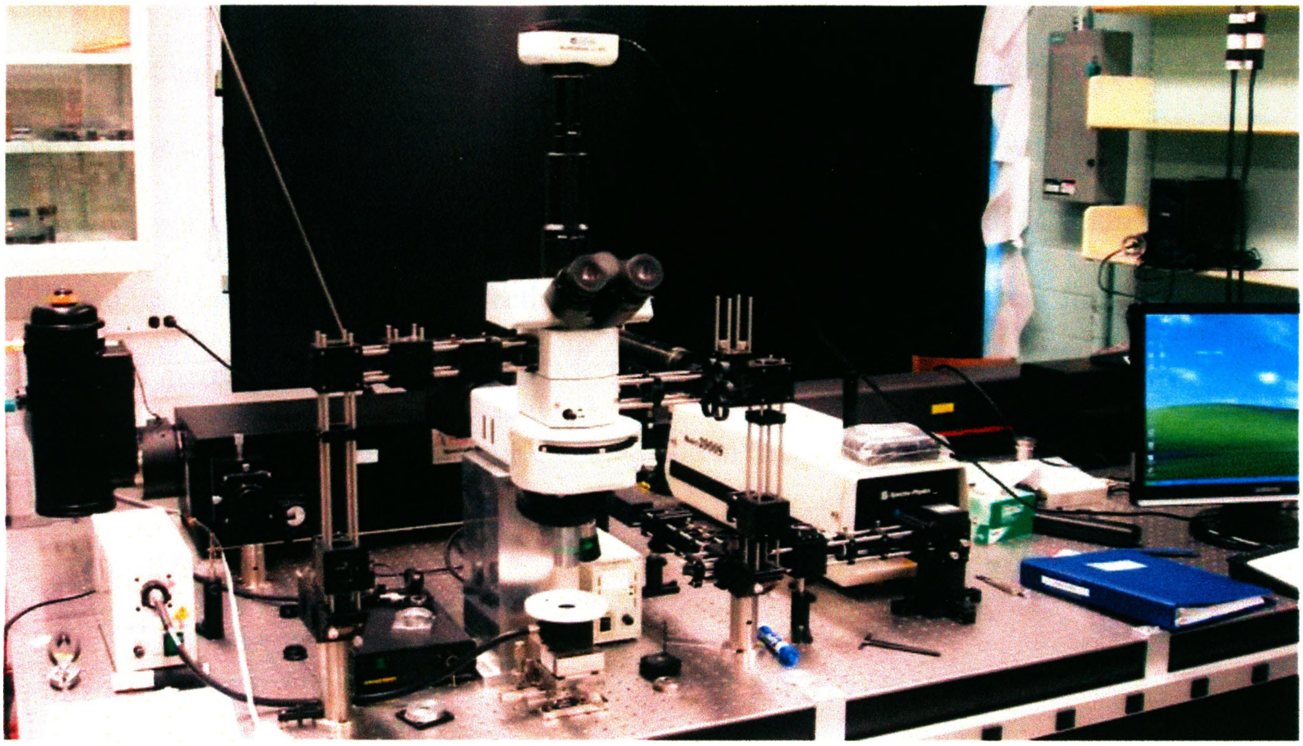

Fig. 1.3 Customized Raman system. A 488 blue laser used as the excitation source was focused on the sample by customized pathways and an objective lens.

Complementary to Raman spectroscopy, IR absorption spectroscopy is mainly based on the absorption of the incident infrared beam in molecules. By absorbing infrared phonons, molecules will be excited to various discrete vibrational or rotational energy levels. Monitoring the absorption can provide spectroscopic data for the vibrations of studied molecules. In our lab, a customized IR microspectroscopy system was used for all room-temperature IR absorption measurements. Fig. 1.4 shows photo of the system. Briefly, a commercial Fourier transform infrared (FTIR) spectrometer from Bruker Optics Inc. (model Vertex 80v) equipped with a Globar IR light source constituted the main component of the micro-IR system, which was operated under a vacuum such that absorption by H_2O and CO_2 was efficiently removed. A collimated IR beam of varying diameter was directed into a relay box through a KBr window onto the spectrometer. The beam was then focused onto the sample in the DAC by an iris optics and a reflective objective lens. The DAC on the sample XYZ precision stage was aligned with the aid of an optical microscope equipped with an objective lens. The transmitted IR beam was collected using another identical reflective objective as the condenser and was directed to a midband mercury cadmium telluride (MCT) detector equipped with a ZnSe window. Again, the detailed experimental set up can be found in Chapters 2 and 3.

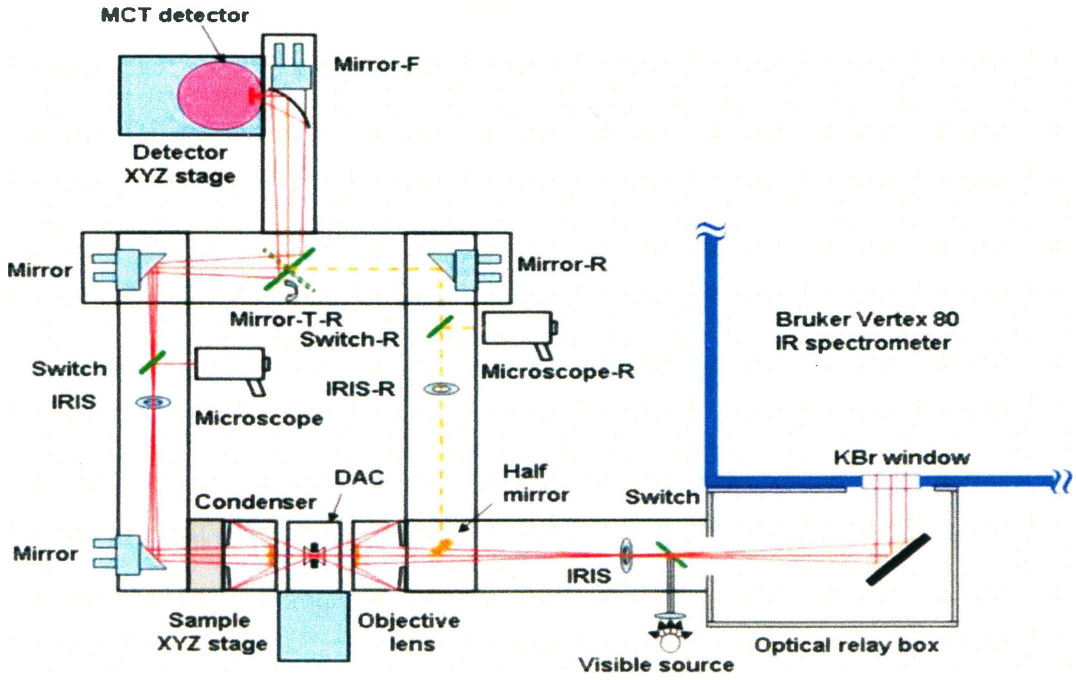

Fig. 1.4 Customized IR system. The spectrometer is equipped with MCT detector and the IR beam is focused on the sample by a microscope objective. (Adapted from Ref. 60)

1.3 High-pressure studies of hydrogen storage materials

Effects of high pressure on the materials provide enhanced opportunities in the formation of novel hydrogen storage systems. Therefore, extensive high-pressure studies have been carried out on hydrogen-containing materials, such as metal hydrides, chemical hydrides and complex systems.[20,22,38] First of all, new hydrides can be obtained by high pressure synthesis using anvil-type apparatus from mixtures.[62-68] For instance, new ternary metal hydrides can be synthesized from binary hydrides in a multi-anvil press.[64] It is also found that some of the species synthesized could be hydrogenated reversibly without disproportionation under high pressure of a few GPa.[67] By adding other metal hydrides, e.g. LiH and NaH, the yield of novel quaternary hydrides $Mg_{7-x}A_xTiH_{16-x}$ (A=Li, Na, K) could be greatly enhanced, which leads to the improvement of reversible hydrogen storage capacities.[68]

The stability and reversibility of potential hydrogen storage materials in different pressure-temperature ranges are important factors that could affect their hydrogen storage performance remarkably. The pressure effects can be monitored by different means such as *in situ* spectroscopy, i.e., Raman and IR spectroscopy. Meanwhile, their structural details and phase transition can be examined by X-ray diffraction measurements. For example, phase transitions of various hydrides, such as MgH_2,[69] BaH_2,[70] $LiBH_4$,[71] α-AlH_3,[72] ErH_3,[73] $NaBH_4$,[74] $Ca(BH_4)_2$[75] and $ErMn_2H_{4.6}$[76] have been identified by X-ray and neutron diffraction. The reversibility of the phase transitions in the studies of different hydrides varies significantly. For instance, all phase transitions of $LiBH_4$ are reversible whereas the transition of $Ca(BH_4)_2$ at 14.4 GPa is reversible but the one between 2.4 and 3.3 GPa is found to be irreversible (irreversible phase transitions indicate its incapability of returning to the original state after the reverse operations, such as decompression).[23,36,61,71]

In addition to the metal hydrides and complex hydrides, recent studies also showed that hydrogen could be stored in some molecular crystals such as in clathrate hydrate under high pressure. For instance, Mao et al.[28] reported that various hydrogen clathrates can be formed upon cooling to 249 K and the compression of a mixture of H_2 and H_2O to around 180-220 MPa. This compound was found to be able to hold 50 $g \cdot L^{-1}$ hydrogen or 5.3 wt%, which can be recovered at ambient pressure up to 145 K. Furthermore, other hydrogen storage systems, such as H_2-CH_4 and H_2-SiH_4 complexes, have also been reported.[28-29] In particular, multiple molecular compounds, $CH_4(H_2)_2$, $(CH_4)_2H_2$, $CH_4(H_2)_4$, were produced at pressures up to10 GPa.[77] For the SiH_4-H_2 system, silane-hydrogen mixtures [$SiH_4(H_2)_2$] with unique intermolecular interactions for hydrogen-rich solids were observed.[78] The spectroscopic and diffraction measurements of the hydrides that have been studied under high pressure so far are summarized in the Table 1.1.

Most of the hydrogen containing complexes above can only be recovered back to original forms at low temperature upon decompression. As a result, simultaneous low temperature and high pressure conditions are important in producing the novel hydrogen materials. It is therefore of great interest to examine the properties of the materials under low temperatures and high pressures *in situ*. In addition, new hydrogen storage materials with improved properties were also synthesized by using combined high pressure and low temperature technologies. For instance, new powders were generated by the ball milling of the $LiNH_2$ + LiH storage system at different low temperatures down to 77 K.[79]

Table 1.1 Summary of previous high-pressure studies on hydrides.

Material	Characterization method	Pressure range	Phase transition pressure (GPa)	Reversibility	Reference
$NaNH_2$	Raman/IR	0-16 GPa	0.9,2.0	Yes	60
$Ca(BH_4)_2$	Raman/IR	0-10.4 GPa	2.3,3.9,6.6	Yes	61
NH_3BH_3	Raman/IR	0-14 GPa	2.4,5.5, 8.5,10.4	Yes	80
B_2H_6	Raman/IR	0-50 GPa	4,6,14	Yes	81-82
SiH_4-H_2	Raman/IR	0-35 GPa	5.7,7.5	N/A	78
$LiBH_4$	Raman/XRD	0-17 GPa	9,16	Yes	71
$NaBH_4$	XRD/ Calculations	0-30 GPa	6-8	N/A	74
BaH_2	Raman/XRD/ Calculations	0-22 GPa	1.6	Yes	70
MgH_2	XRD/ Calculations	0-16 GPa	0.4,3.8,10.2	N/A	69
CH_4-H_2	XRD/Raman/ Visual	0-30 GPa	5.4,8.1	N/A	77

1.4 Motivation and thesis structure

Among the many hydrogen storage materials mentioned above, two materials, sodium amide ($NaNH_2$) and ammonia borane (NH_3BH_3), were studied by me under high pressure by vibrational spectroscopy. Both materials of my project, sodium amide ($NaNH_2$)[60] and ammonia borane (NH_3BH_3)[80,83] are known promising hydrogen storage materials. There have been extensive studies on their structures, stabilities and reactivities at ambient pressure and room temperature. However, the high pressure induced structural transformations of $NaNH_2$ and simultaneous high-pressure and low-temperature induced phase transitions of NH_3BH_3 have not been examined and understood. Thus, the understanding of the structures and stabilities of $NaNH_2$ and NH_3BH_3 under high pressure and low temperature conditions is of great importance for further applications of these materials in hydrogen storage.

The main theme of my thesis is to examine the structures and properties of $NaNH_2$ under high pressures and NH_3BH_3 under high pressures and low temperatures using DAC technology by Raman and IR spectroscopies. Several phase transformations are observed and possible structures, stabilities and reversibilities of $NaNH_2$ and NH_3BH_3 are proposed under high pressures and low temperatures. The detailed discussion is shown in Chapter 2 and Chapter 3, respectively. The $NaNH_2$ work has been published in the Journal of Physical Chemistry B 2011, *115*, 7, while the NH_3BH_3 work has been submitted to the Journal of Physical Chemistry C. Moreover, we conducted *in situ* synchrotron X-ray high pressure studies on $NaNH_2$ at High Pressure Collaborative Access Team (HPCAT) of advanced photon source of Argonne National Lab. Selected 2-

D X-ray spectra are reported in the Appendix. Finally, the summary and suggestions for future work are included in Chapter 4.

1.5 References

(1) Materials Science Correspondent. *Nature* **1973**, *243*, 184.

(2) Bockris, J. O. M. *Science* **1972**, *176*, 1323.

(3) Bockris, J. O. M. *Int. J. Hydrogen Energ.* **2002**, *27*, 731.

(4) Masel, R. *Nature* **2006**, *442*, 521.

(5) Zuttel, A. *Naturwissenschaften* **2004**, *91*, 157.

(6) Stetson, N. T.; Read, C.; Ordaz, G.; Gardiner, M.; Dillich, S. *Abstr .Pap. Am. Chem. S.* **2009**, *238.*

(7) Satyapal, S.; Petrovic, J.; Read, C.; Thomas, G.; Ordaz, G. *Catal. Today* **2007**, *120*, 246.

(8) Brattain, W. H.; Gunsul, C. J. W. *Science* **1974**, *186*, 302.

(9) Darkrim, F. L.; Malbrunot, P.; Tartaglia, G. P. *Int. J. Hydrogen Energ* **2002**, *27*, 193.

(10) Cohen, R. L.; Wernick, J. H. *Science* **1981**, *214*, 1081.

(11) Dillon, A. C.; Jones, K. M.; Bekkedahl, T. A.; Kiang, C. H.; Bethune, D. S.; Heben, M. J. *Nature* **1997**, *386*, 377.

(12) Gogotsi, Y.; Portet, C.; Osswald, S.; Simmons, J. M.; Yidirim, T.; Laudisio, G.; Fischer, J. E. *Int. J. Hydrogen Energ* **2009**, *34*, 6314.

(13) Heben, M. J.; Dillon, A. C. *Science* **2000**, *287*, 593.

(14) Lin, J. Y. *Science* **2000**, *287*, 1929.

(15) Liu, C.; Fan, Y. Y.; Liu, M.; Cong, H. T.; Cheng, H. M.; Dresselhaus, M. S.

Science **1999**, *286*, 1127.

(16) Nishihara, H.; Hou, P. X.; Li, L. X.; Ito, M.; Uchiyama, M.; Kaburagi, T.; Ikura, A.; Katamura, J.; Kawarada, T.; Mizuuchi, K.; Kyotani, T. *J. Phys. Chem. C* **2009**, *113*, 3189.

(17) Graetz, J. *Chem. Soc. Rev.* **2009,** *38*, 73.

(18) Kazemian, H.; Lim, K. L.; Yaakob, Z.; Daud, W. R. W. *Chem. Eng .Technol* **2010**, *33*, 213.

(19) Rosi, N. L.; Eckert, J.; Eddaoudi, M.; Vodak, D. T.; Kim, J.; O'Keeffe, M.; Yaghi, O. M. *Science* **2003**, *300*, 1127.

(20) Sakintuna, B.; Lamari-Darkrim, F.; Hirscher, M. *Int. J. Hydrogen Energ.* **2007**, *32*, 1121.

(21) Wang, Q.; Chen, Y. U.; Tao, M. D.; Wu, C. L. *Rare Metal. Mat. Eng.* **2008,** *37*, 382.

(22) Jain, I. P.; Jain, P.; Jain, A. *J. Alloy. Compd.* **2010**, *503*, 303.

(23) Kim, J. H.; Jin, S. A.; Shim, J. H.; Cho, Y. W. *Scripta Mater.* **2008**, *58*, 481.

(24) Lin, Y.; Mao, W. L.; Mao, H. K. *P. Natl. Acad. Sci. USA* **2009**, *106*, 8113.

(25) Srinivasan, S. S.; Niemann, M. U.; Phani, A. R.; Kumar, A.; Goswami, D. Y.; Stefanakos, E. K. *J. Nanomater* **2008,** *10*, 1155.

(26) Xiong, Z. T.; Yong, C. K.; Wu, G. T.; Chen, P.; Shaw, W.; Karkamkar, A.; Autrey, T.; Jones, M. O.; Johnson, S. R.; Edwards, P. P.; David, W. I. F. *Nat. Mater.* **2008**, *7*, 138.

(27) Lee, H.; Lee, J. W.; Kim, D. Y.; Park, J.; Seo, Y. T.; Zeng, H.; Moudrakovski, I. L.; Ratcliffe, C. I.; Ripmeester, J. A. *Nature* **2005**, *434*, 743.

(28) Mao, W. L.; Mao, H. K.; Goncharov, A. F.; Struzhkin, V. V.; Guo, Q. Z.; Hu, J. Z.; Shu, J. F.; Hemley, R. J.; Somayazulu, M.; Zhao, Y. S. *Science* **2002**, *297*, 2247.

(29) Strobel, T. A.; Somayazulu, M.; Hemley, R. J. *Phys. Rev. Lett* .**2009**, *103*, 065701.

(30) Wang, P.; Kang, X. D.; Cheng, H. M. *J. Phys. Chem. C* **2007**, *111*, 4879.

(31) Kang, J. K.; Lee, J. Y.; Muller, R. P.; Goddard, W. A. *J. Chem. Phys.* **2004**, *121*, 10623.

(32) Vajeeston, P.; Ravindran, P.; Vidya, R.; Fjellvag, H.; Kjekshus, A. *Phys. Rev. B* **2003**, *68*, 212101.

(33) Principi, G.; Barison, S.; Agresti, F.; Lo Russo, S.; Maddalena, A.; Palade, P.; Torzo, G. *J. Alloy. Compd.* **2008**, *459*, 343.

(34) Shaw, L. L.; Markmaitree, T.; Osborn, W. *Int. J. Hydrogen Energ* **2008**, *33*, 3915.

(35) Luo, W. F. *J. Alloy. Compd.* **2004**, *381*, 284.

(36) Sudik, A.; Yang, J.; Halliday, D.; Wolverton, C. *J. Phys. Chem. C* **2008**, *112*, 4384.

(37) Biniwale, R. B.; Rayalu, S.; Devotta, S.; Ichikawa, M. *Int. J. Hydrogen Energ* **2008**, *33*, 360.

(38) Matthews, M. A.; Davis, T.; Marrero-Alfonso, E. Y. *Abstr. Pap. Am. Chem. S.* **2004**, *228*, 678.

(39) Wu, H.; Zhou, W. *Abstr. Pap. Am. Chem. S.* **2009**, *237*, 255.

(40) *Website: http://en.wikipedia.org/wiki/High_pressure.*

(41) Weir, C. E.; Lippincott, E. R.; Vanvalkenburg, A.; Bunting, E. N. *J. Res. Nbs. a Phys. Ch.* **1959**, *63*, 55.

(42) Hemley, R. J.; Mao, H.; Cohen, R. E. *Rev. Mineral* **1998**, *37*, 591.

(43) Desgreniers, S.; Vohra, Y. K.; Ruoff, A. L. *J. Phys. Chem.* **1990**, *94*, 1117.

(44) Weir, S. T.; Mitchell, A. C.; Nellis, W. J. *Phys. Rev. Lett.* **1996**, *76*, 1860.

(45) Mao, W. L.; Mao, H. K.; Eng, P. J.; Trainor, T. P.; Newville, M.; Kao, C. C.; Heinz, D. L.; Shu, J. F.; Meng, Y.; Hemley, R. J. *Science* **2003**, *302*, 425.

(46) Yan, C. S.; Mao, H. K.; Li, W.; Qian, J.; Zhao, Y. S.; Hemley, R. J. *Phys Status Solidi A* **2004**, *201*, R25.

(47) Yoo, C. S.; Cynn, H.; Gygi, F.; Galli, G.; Iota, V.; Nicol, M.; Carlson, S.; Hausermann, D.; Mailhiot, C. *Phys .Rev. Lett.***1999**, *83*, 5527.

(48) Deemyad, S.; Schilling, J. S. *Phys. Rev. Lett.* **2003**, *91*, 167001.

(49) Shimizu, K.; Suhara, K.; Ikumo, M.; Eremets, M. I.; Amaya, K. *Nature* **1998**, *393*, 767.

(50) Struzhkin, V. V.; Eremets, M. I.; Gan, W.; Mao, H. K.; Hemley, R. J. *Science* **2002**, *298*, 1213.

(51) Hemley, R. J.; Mao, H. K. *Aip. Conf. Proc.* **2004**, *706*, 17.

(52) Block, S.; Piermarini, G. *Phys. Today* **1976**, *29*, 44.

(53) Block, S.; Piermarini, G. *Usp Fiz Nauk* **1979**, *127*, 705.

(54) Jayaraman, A. *Rev. Mod. Phys.* **1983**, *55*, 65.

(55) Zou, G. T.; Ma, Y. Z.; Mao, H. K.; Hemley, R. J.; Gramsch, S. A. *Rev. Sci. Instrum* **2001**, *72*, 1298.

(56) Bassett, W. A.; Shen, A. H.; Bucknum, M.; Chou, I. M. *Rev. Sci. Instrum* **1993**, *64*, 2340.

(57) Schiferl, D. *Rev. Sci. Instrum.* **1987**, *58*, 1316.

(58) Mao, H. K.; Xu, J.; Bell, P. M. *J. Geophys. Res-Solid* **1986**, *91*, 4673.

(59) Yen, J.; Nicol, M. *J. Appl. Phys.* **1992**, *72*, 5535.

(60) Liu, A.; Song, Y. *J. Phys. Chem. B* **2011**, *115*, 7.

(61) Liu, A.; Xie, S. T.; Dabiran-Zohoory, S.; Song, Y. *J. Phys. Chem. C* **2010**, *114*, 11635.

(62) Hemmes, H.; Driessen, A.; Kos, J.; Mul, F. A.; Griessen, R.; Caro, J.; Radelaar, S. *Rev. Sci. Instrum.* **1989**, *60*, 474.

(63) Goto, Y.; Kakuta, H.; Kamegawa, A.; Takamura, H.; Okada, M. *Mater. Trans.* **2001**, *42*, 1850.

(64) Kohlmann, H.; Bertheville, B.; Hansen, T.; Yvon, K. *J. Alloy Compd.* **2001**, *322*, 59.

(65) Takamura, H.; Kakuta, H.; Goto, Y.; Kamegawa, A.; Okada, M. *Mater. Trans.* **2001**, *42*, 1301.

(66) Kamegawa, A.; Goto, Y.; Kakuta, H.; Takamura, H.; Okada, M. *J. Alloy Compd.* **2006**, *408*, 284.

(67) Kataoka, R.; Kamegawa, A.; Takamura, H.; Okada, M. *Mater. Trans.* **2009**, *50*, 1179.

(68) Takasaki, T.; Mukai, T.; Kitamura, N.; Tanase, S.; Sakai, T. *J. Alloy. Compd.* **2010**, *494*, 439.

(69) Vajeeston, P.; Ravindran, P.; Hauback, B. C.; Fjellvag, H.; Kjekshus, A.; Furuseth, S.; Hanfland, M. *Phys. Rev. B* **2006**, *73*, 224102.

(70) Smith, J. S.; Desgreniers, S.; Tse, J. S.; Klug, D. D. *J. Appl. Phys.* **2007**, *102*, 043520.

(71) Filinchuk, Y.; Chernyshov, D.; Nevidomskyy, A.; Dmitriev, V. *Angew Chem Int. Edit* **2008**, *47*, 529.

(72) Graetz, J.; Chaudhuri, S.; Lee, Y.; Vogt, T.; Muckerman, J. T.; Reilly, J. J. *Phys. Rev. B* **2006**, *74*, 214114.

(73) Palasyuk, T.; Tkacz, M. *Solid State Commun.* **2004**, *130*, 219.

(74) Kim, E.; Kumar, R.; Weck, P. F.; Cornelius, A. L.; Nicol, M.; Vogel, S. C.; Zhang, J. Z.; Hartl, M.; Stowe, A. C.; Daemen, L.; Zhao, Y. S. *J. Phys. Chem. B* **2007**, *111*, 13873.

(75) George, L.; Drozd, V.; Saxena, S. K.; Bardaji, E. G.; Fichtner, M. *J. Phys. Chem. C* **2009**, *113*, 15087.

(76) Makarova, O. L.; Goncharenko, I. N.; Le Bihan, T. *Solid State Commun.* **2004**, *132*, 329.

(77) Somayazulu, M. S.; Finger, L. W.; Hemley, R. J.; Mao, H. K. *Science* **1996**, *271*, 1400.

(78) Strobel, T. A.; Somayazulu, M.; Hemley, R. J. *Phys. Rev. Lett.* **2009**, *103*, 065701.

(79) Osborn, W.; Markmaitree, T.; Shaw, L. L.; Hu, J. Z.; Kwak, J.; Yang, Z. G. *Int. J. Hydrogen Energ* **2009**, *34*, 4331.

(80) Xie, S. T.; Song, Y.; Liu, Z. X. *Can. J. Chem.* **2009**, *87*, 1235.

(81) Murli, C.; Song, Y. *J. Phys. Chem. B* **2009**, *113*, 13509.

(82) Song, Y.; Murli, C.; Liu, Z. X. *J. Chem. Phys.* **2009**, *131*, 174506.

(83) Liu, A.; Song, Y. *J. Phys .Chem. C* **2011**, *submitted.*

Chapter 2 *In situ* high-pressure study of sodium amide by Raman and IR spectroscopy

A version of this chapter has been published in *J. Phys. Chem. B* **2011**, *115*, 7.

2.1 Introduction

Recently, there have been intensive research and significant developments in condensed-phase hydrogen storage materials.[1-10] In particular, many studies have focused on lightweight metal hydrides, such as LiH, MgH_2, $LiBH_4$, and $LiNH_2$, etc., due to their outstanding properties for practical applications.[11-12] For instance, lithium amide ($LiNH_2$) with a high gravimetric hydrogen density (18.5 wt%) has exhibited safe, efficient and reversible hydrogen storage capacities, and thus has been studied extensively.[13-15] Another alkaline amide in the same group, sodium amide ($NaNH_2$), has also demonstrated promising hydrogen storage capacities. Although $NaNH_2$ has a relatively lower hydrogen content (5.2 wt%), a recent study shows that $NaNH_2$ played an important role to facilitate hydrogen release with other metal hydrides (e.g. $LiAlH_4$) by forming intermediate hydride complexes via ball milling.[16] Compared to $LiNH_2$, however, $NaNH_2$ has not been studied that well yet and as a result, very little is known about its structures or solid state reactivities in a broad temperature or pressure range that is important for hydrogen storage applications.

Sodium amide, one of the light-weight metal hydrides (density: 1.39 g/cm^3), crystallizes into an orthorhombic cell at ambient conditions with space group *Fddd* (D_{2h}^{24}) and cell parameters a=8.964 Å, b=10.456 Å, c=8.073 Å and Z=16.[17] The unit cell structure of $NaNH_2$ is shown in Fig. 2.1. The sodium and amide ions occupy respective

Wyckoff positions (In crystallography, a Wyckoff position is a point belonging to a set of points for which site symmetry groups are conjugate subgroup of the space group) of 16*f* and 16*g*, thus forming a sodium-centered tetrahedral coordination with a Na-N distance of 2.4-2.5 Å.

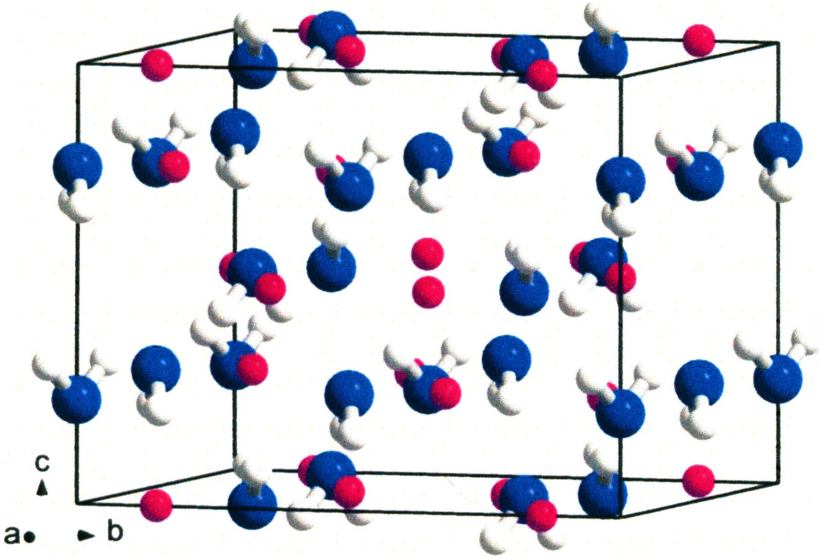

Fig. 2.1 Ambient-pressure crystal structure of $NaNH_2$ in space group *Fddd.* The coordinate system is indicated to show the orientations of the unit cell. The color codes for atoms are pink (sodium), blue (nitrogen), and white (hydrogen).

In amide/imide systems, possible hydrogen bonding is typically considered an important factor affecting structures and properties of these materials. However, the specific orientation of amide anions and the closest intermolecular nitrogen-hydrogen distance of 3.56 Å in the unit cell do not seem to facilitate the formation of effective hydrogen bondings. In 1972, Cunningham et al. reported the Raman spectra of solid and molten $NaNH_2$.[18] Isoelectronic with H_2O, NH_2^- ion has a simple C_{2v} symmetry thus giving three fundamental bands observed and assigned as 3218 cm^{-1} [$\nu_1(A_1)$, symmetric stretch], 1550 cm^{-1} [$\nu_2(A_1)$, bending], and 3267 cm^{-1} [$\nu_3(B_2)$, asymmetric stretch]. The sharp band profile of the fundamental modes of the NH_2^- ions indicated that there is little, if any, hydrogen bonding among NH_2^- ions in either liquid or solid $NaNH_2$, consistent with the crystal structure.

Since the high-pressure technique has demonstrated an effective approach to produce new structures with possibly enhanced hydrogen storage capacities, a wide variety of hydride complexes (e.g., ammonia borane, diborane, calcium borohydride) have been investigated under high pressures.[19-22] In addition, ball milling as a prevailing approach of preparing hydrogen storage materials is a process of driving chemical and structural transformations by external pressure tuning. Therefore, in-depth investigation of the structures, properties and transformations of these potential hydrogen storage materials provides important insight into the understanding of the reaction mechanisms involving hydrogen discharge/recharge and thus subsequent practical applications in hydrogen storage. Under this context, Chellappa et al. recently performed *in situ* high-pressure Raman spectroscopic studies on $LiNH_2$ up to 25 GPa.[23] A pressure-induced phase transition was observed to start at 12 GPa and to complete at 14 GPa as characterized by the splitting of the fundamental modes. The new high-pressure phase (labeled as β-$LiNH_2$) was believed to have a different crystal structure containing orientationally ordered amide anions than the original α-phase $LiNH_2$. However, the corresponding high-pressure study on $NaNH_2$ has not yet been conducted.

In this study, we report the first *in situ* high-pressure Raman and IR measurements on $NaNH_2$, which were compressed up to 10 GPa and 15 GPa in diamonds anvil cells (DACs), respectively. We observed pressure-induced transformations in strong contrast to those observed for $LiNH_2$. These findings may help to understand the different roles of $LiNH_2$ and $NaNH_2$ in their hydrogen storage applications.

2.2 Experimental Section

2.2.1 Sample preparation

Sodium amide as a fine gray powder with ~ 95% purity was purchased from Sigma-Aldrich and used without further purification. A symmetrical DAC with two type-I diamonds (containing nitrogen atoms as main impurities) with 400 μm culets was used for the high-pressure Raman measurements, while a pair of type-II diamonds (no measurable nitrogen impurities) with a culet size of 600 μm was used for the IR measurements. The sample loading was performed in an MBraun LAB Master 130 glovebox filled with N_2 atmosphere (< 10 ppm O_2 and H_2O) and without any fluid pressure-transmitting medium to accommodate the hygroscopicity of the material. A few ruby (Cr^{3+} doped α-Al_2O_3) chips as the pressure calibrant were carefully placed inside the sample chamber before the sample was loaded. The pressure was determined by using the R_1 ruby fluorescence line shift with an accuracy of ± 0.05 GPa under quasi-hydrostatic conditions.[24] For IR measurements, spectral quality KBr powders used both as pressure transmitting medium and to dilute the sample were also loaded into the DAC. In the entire pressure region, ruby fluorescence spectra obtained on different ruby chips across the sample chamber indicated no significant pressure gradient or non-hydrostatic effect.

2.2.2 High-pressure Raman measurements

A customized Raman micro-spectroscopy system was used to collect the Raman spectra. A 488 nm line from an Innova Ar^+ laser (Coherent Inc.) was used as the excitation source. The laser was focused to < 5 μm on the sample by a 20× Mitutoyo objective. The Raman signal was detected with backscattering geometry by the same objective lens. The Rayleigh scattering was removed by a pair of notch filters that enabled a spectral range > 100 cm^{-1} to be measured. The scattered light was then dispersed using an imaging spectrograph equipped with an 1800 lines/mm grating achieving a 0.1 cm^{-1} resolution. The Raman signal was recorded using an ultrasensitive, liquid nitrogen cooled, back-illuminated, charge-coupled device (CCD) detector from Acton. The system was calibrated by neon lines with an uncertainty of ± 1 cm^{-1}. To avoid the strong first-order Raman mode of diamond at 1334 cm^{-1}, the spectra were collected in ranges of 100-1300 cm^{-1} and 1350-3400 cm^{-1} in several collection windows. For each spectrum, a collection time of 30 s was employed, and the average laser power on the sample was maintained at ~ 30 mW. All Raman measurements were conducted at room temperature and pressures of up to ~ 10 GPa, and were reproduced several times.

2.2.3 High-pressure IR measurements

A customized IR micro-spectroscopy system was used for all room-temperature IR absorption measurements; the detailed instrumentation has been described elsewhere.[25] Briefly, a commercial Fourier transform infrared (FTIR) spectrometer from Bruker Optics Inc. (Model Vertex 80v) equipped with Globar mid-IR light source constituted the main component of the micro-IR system, which was operated under a vacuum of < 5 mbar, such that the absorption by H_2O and CO_2 was efficiently removed. A collimated IR beam was directed into a relay box through a KBr window on the spectrometer. The beam was then focused onto the sample in the DAC by an iris optics and 15× reflective objective lens with a numerical aperture of 0.4. The size of the IR beam was set to be identical to the entire sample size (e.g., ~ 150 μm) by a series of iris apertures. The transmitted IR beam was collected using another identical reflective objective as the condenser, and was directed to a wide-band mercury cadmium telluride (MCT) detector equipped with a ZnSe window that allows measurements in the spectral range of 400 to 10000 cm^{-1}. All measurements were undertaken in transmission (or absorption) mode. A resolution of 4 cm^{-1} and 512 scans were applied for each spectrum measurement achieving an excellent signal-to-noise ratio. The reference spectrum, i.e., the absorption of diamond anvils loaded with KBr but without any sample, was later divided as background from each sample spectrum to obtain the absorbance.

2.3 Results and Discussion

2.3.1 Ambient-pressure Raman and IR spectra.

Raman and IR spectra were collected at ambient conditions as a starting point and are shown in Fig. 2.2. The C_{2v} point group symmetry of NH_2^- predicts that all three vibrational bands ($2A_1 + B_2$) are both Raman and IR active. As expected, three fundamental internal modes were observed at 1539, 3218 and 3269 cm^{-1} in the Raman spectrum, corresponding to the bending mode ν_2 (A_1), the N-H symmetric stretching mode ν_1 (A_1), and N-H asymmetric stretching mode ν_3 (B_2), respectively. The corresponding IR bands appeared at slightly lower frequencies: 1530, 3212 and 3259 cm^{-1}. The sharp Raman modes of NH_2^- ion are in marked contrast to the Raman spectra of water,[26-28] where aggregated H_2O molecules linked by hydrogen bonds cause extensive broadening of the fundamentals in both solid and liquid phases. Our measurements are in excellent agreement with the Raman study by Cunningham[18] and the IR study by Nibler et al.[29] on the condensed phase of $NaNH_2$, as can be seen from Table 2.1. We also list the vibrational frequencies of NH_2^- with the other moiety being Li^+ as reported by Bohger et al.[30] All the frequencies of the internal modes of NH_2^- are higher in $LiNH_2$ than in $NaNH_2$, indicating that NH_2^- group in $LiNH_2$ is characterized with shorter N-H distance and thus higher bond stiffness.

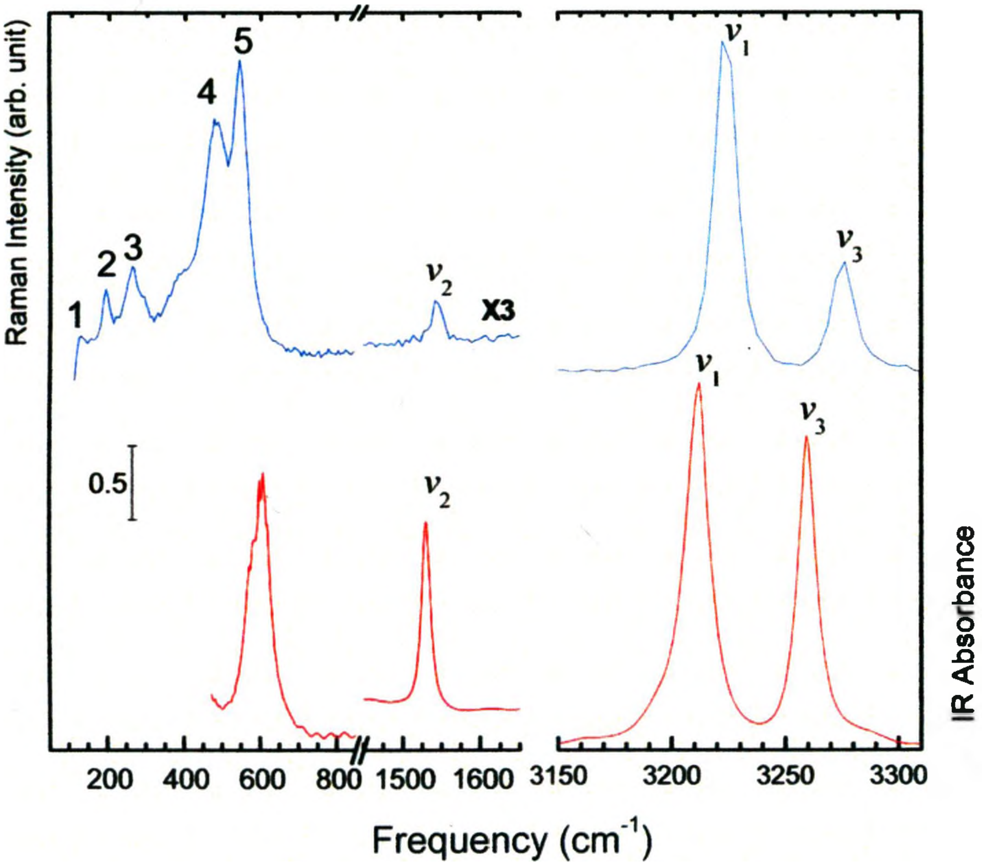

Fig. 2.2 Raman spectrum of $NaNH_2$ (top) in comparison with IR spectrum (bottom) in the spectral region 100-3300 cm^{-1}, both collected at near-ambient pressure and room temperature. The omitted spectral regions are due to the lack of spectroscopic features. The vertical bar labels the scale of the absolute absorbance intensity. The assignment of the vibational modes is labeled above each band.

In addition, we observed five Raman bands at 115, 177, 251, 464 and 535 cm^{-1} which we label as 1, 2, 3, 4, 5, respectively, and one IR band at 609 cm^{-1} in the lattice region. On the basis of the factor group analysis using the established crystal structure of $NaNH_2$, 33 lattice vibrational (21 translational and 12 librational) modes are expected, among which 18 are Raman active and 12 are IR active. Apparently, the observed lattice modes are just a subset of the total predicted modes. The limit of the notch filter used in the Raman measurements and the spectral limit of > 400 cm^{-1} imposed by our IR instrument capability may also contribute to the lack of the lattice modes observed. Cunningham reported even fewer lattice modes for solid $NaNH_2$ at 522, 468 and 349 cm^{-1}, in rough agreement with our results.[18] Using neutron scattering, Day and Sinclair investigated the vibrational modes of $NaNH_2$ as well, e.g., weak $[NH_2]^-$ torsion at ~ 400 cm^{-1}, a strong wagging peak at 550 cm^{-1} and a broad peak due to rocking at 1000 cm^{-1}.[31] Some strong bands at 560/550 cm^{-1} and a small bump at 400 cm^{-1} were observed in the lattice region, which were attributed to NH_2^- torsion and wagging respectively. All these comparisons are summarized in Table 2.1 as well. We therefore tentatively assign Raman lattice modes 1-3 as translational modes and modes 4 and 5 as well as the IR lattice mode as librational modes.

Table 2.1 Vibrational frequencies (cm^{-1}) of $NaNH_2$ at Ambient Pressure.

Mode	Description	This work		Reference				
		Raman	IR	Solid[a]	Liquid[a]	IR[b]	Raman[c]	IR[c]
ν_1	Symmetric stretch	3210	3212	3218	3218	3212	3258	3258
ν_2	Bending	1536	1530	1531	1550	1539	1561	1539
ν_3	Asymmetric stretch	3261	3259	3267	3267	3263	3315	3310
5	Lattice modes	535	609	522	789	560/550[d]		
4		464		468	506	400[d]		
3		251		349	283			
2		177						
1		115						

[a] Reference 18, Raman measurements. [b] Reference 29.

[c] Reference 30, measured for $LiNH_2$. [d] Reference 31, using neutron scattering (see text).

2.3.2. Raman spectra on compression.

Starting from ambient pressure, Raman spectra of $NaNH_2$ were collected upon compression to 10.3 GPa with selected spectra depicted in Fig. 2.3. As can be seen, all the lattice modes were significantly weakened when compressed from ambient pressure to ~0.9 GPa, especially for the librational modes (modes 4 and 5). Above 0.9 GPa, lattice mode 3 was found to split together with the depletion of mode 2 and 4. All these observations strongly suggest a phase transition associated with significant modification of the crystal structure of $NaNH_2$. Concurrently, the ν_2 H-N-H bending mode exhibited a prominent intensity reduction and apparently developed into a doublet at 0.9 GPa, reinforcing the phase transition evidenced by the lattice modes at this pressure. The most dramatic changes were observed in the ν_1 and ν_3 stretching modes. In particular, the ν_1 mode displayed a shoulder which rapidly developed into a doublet around 0.9 GPa. Further compression resulted in the resolution of a third component together with the weakening of the original component of this mode (e.g., at 1.73 GPa). We labeled these multiple components of this mode with ν_1, $\nu_{1A,}$ ν_{1B} and ν_{1C} in the order of their appearing sequence. Similarly, the ν_3 mode first split into a doublet around 0.9 GPa which subsequently evolved into a triplet as well (e.g., at 1.73 GPa) and the multiple components were labeled in a similar way as the ν_1 mode (Fig. 2.3B). When compressed to ~ 2 GPa, another round of changes in the entire spectral region was observed. First of all, no obvious lattice modes were observed above 2 GPa; the ν_2 bending mode was also completely depleted. Furthermore, the obvious characteristic of the stretching modes is the component merging and band broadening. For example, the ν_1 mode displayed a singlet with a front shoulder at 5.3 GPa whereas the ν_3 mode appeared as a single broad band. At the highest pressure of the current study (i.e. 10.3 GPa), all bands became extremely weak and broad with only one dominant peak (i.e., the ν_1 mode) observable.

Table 2.2 Pressure Dependence of the Optical Modes of $NaNH_2$ on Compression [a]

Optical Mode	Frequency (cm^{-1}) [b]	$d\nu/dP$ (cm^{-1}·GPa^{-1})[c]		
		Phase I (<0.9 GPa)	Phase II [d] (0.9-2.0 GPa)	Phase III (>2.0 GPa)
ν_3	3261(3259)	10.6 (9.6)	11.0 (12.2)	7.0 (6.8)
			9.8 (8.4)	7.4 (7.6)
			6.9 (7.7)	6.8
ν_1	3210(3212)	11.7 (9.9)	9.5 (10.2)	6.5
			9.9 (8.8)	6.8 (6.6)
			7.1 (7.6)	
ν_2	1536(1530)	4.9 (0)	1.3 (3.0)	(3.4)
			(1.5)	(1.0)

[a] Values refer to Raman modes while those in parentheses refer to IR modes. [b] Measured at ambient pressure and room temperature. [c] Multiple entries for each mode correspond to the splittings (see Fig. 2.3-2.6). [d] Quadratic regression was used for Raman modes in this phase and the values correspond to average $d\nu/dP$ in this pressure region.

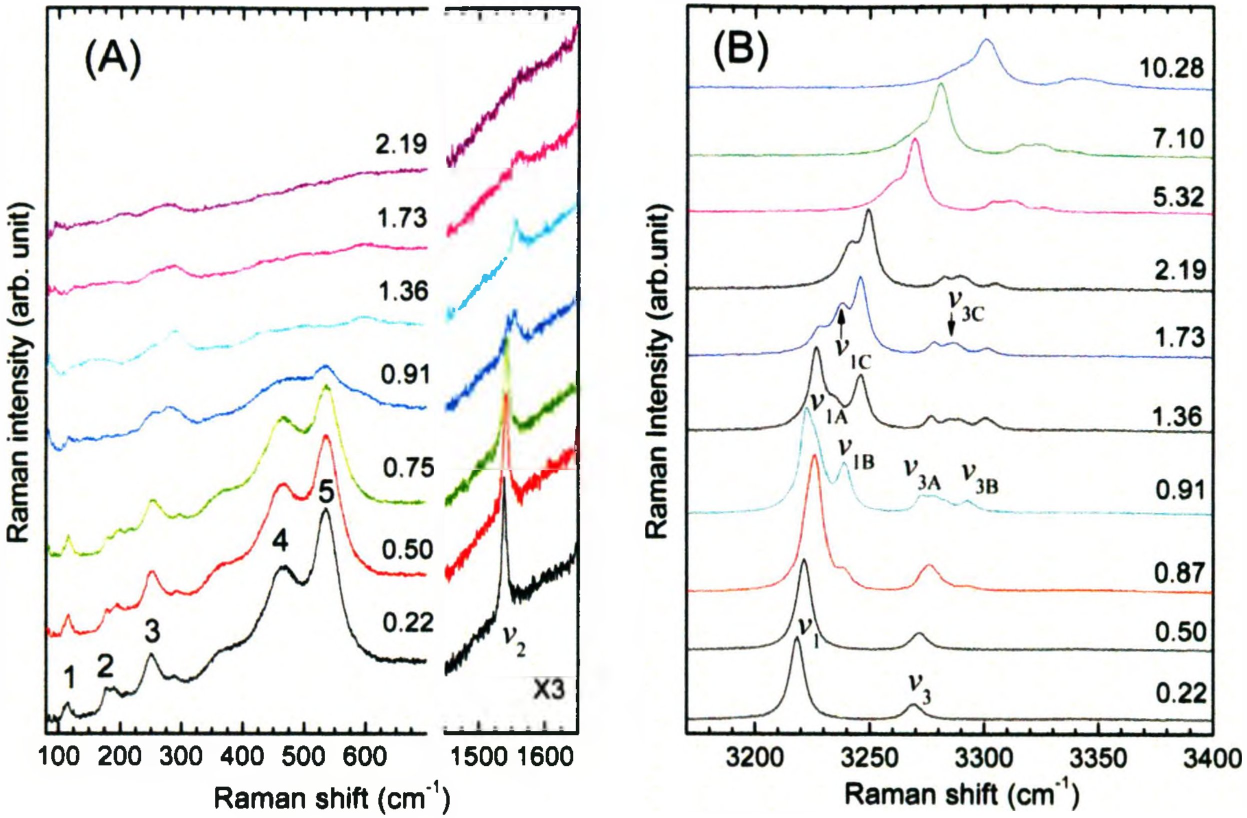

Fig. 2.3 Selected Raman spectra of $NaNH_2$ collected at room temperature on compression in the regions 100-1650 cm-1 at pressures of 0.22-2.19 GPa (A) and 3150-3400 cm^{-1} at pressures of 0.22-0.28 GPa (B). The relative intensities are normalized and thus are directly comparable. The pressures in GPa are labeled for each spectrum. The assignments are labeled for selected Raman modes (see text).

2.3.3. IR spectra on compression.

Mid-IR spectra of $NaNH_2$ were collected on compression to 15.7 GPa. Selected absorption spectra as a function of pressure in the spectral region of 500-3400 cm^{-1} are depicted in Fig. 2.4. Overall, all bands became significantly broadened with increasing pressure. In the lattice region, specifically, the librational mode at ~ 600 cm^{-1} first became weakened and broadened when compressed from ambient pressure to ~ 1 GPa, followed by the complete depletion at ~ 2 GPa, above which pressure an extremely broad IR band was observed in this region all the way to the highest pressure. In contrast, the ν_2 bending mode of the amide anion was found to split into a doublet (labeled as ν_{2A} and ν_{2B}) when compressed to ~ 1 GPa. Above 2 GPa, this mode exhibited an abrupt broadening for both components and enhanced separation with progressive compressions. Similar to the Raman measurements, the ν_1 and ν_3 IR modes were also found to split with compression. For example, both modes split into a doublet (labeled as ν_{1A}/ν_{1B} and ν_{3A}/ν_{3B}) which each rapidly evolved into a triplet. Above 2 GPa, the multiple components for both modes started to merge, for example, into a broad singlet for ν_1 mode and a doublet for ν_3 mode. When the pressure is sufficiently high, e.g., at ~ 7 GPa, both stretching modes displayed a singlet again as at ambient pressure, except that the bandwidths are much larger.

In summary, these IR spectroscopic observations collectively suggest that $NaNH_2$ underwent phase transitions at ~ 1 GPa and ~ 2 GPa, consistent with those identified by Raman measurements. No further dramatic phase transitions were observed up to the highest pressure achieved, indicating that the third high-pressure phase has a much larger stability region than the previous two.

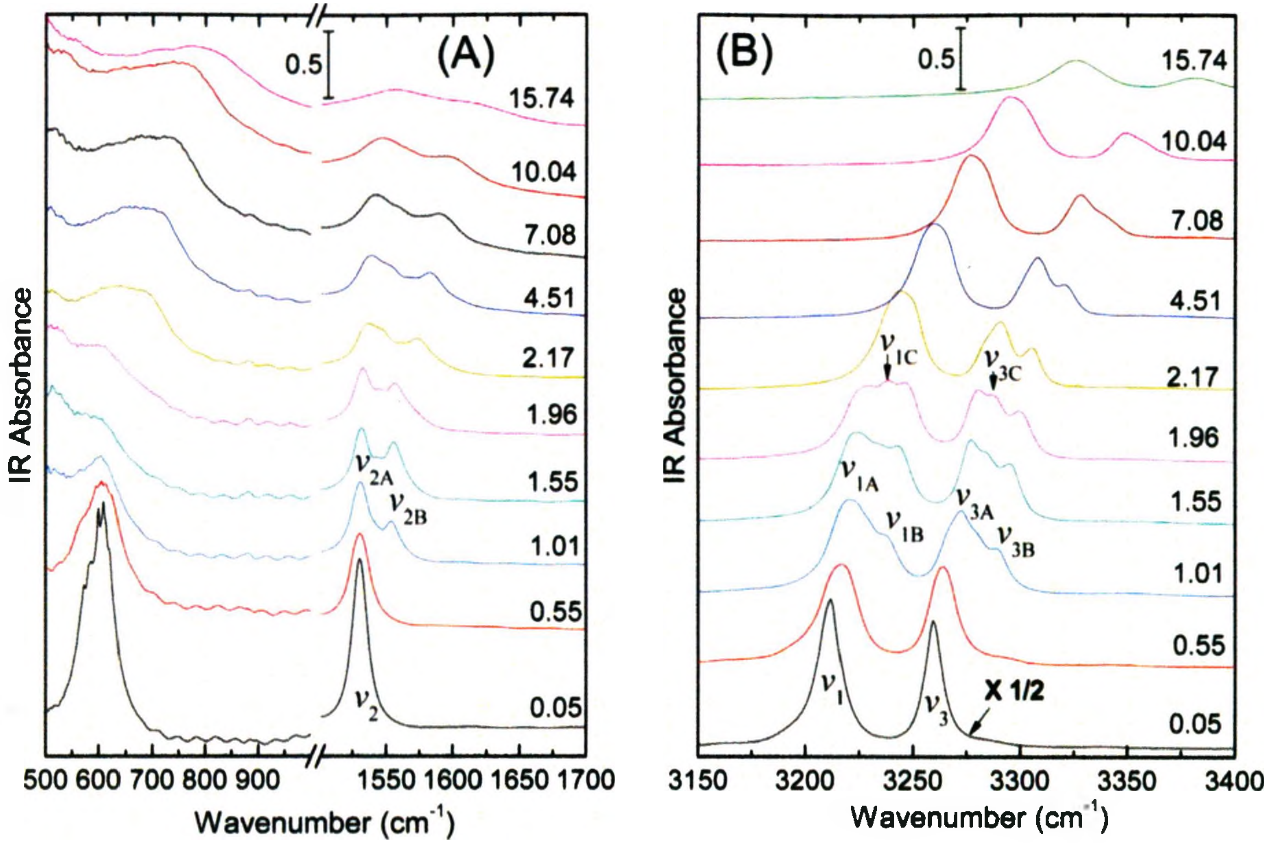

Fig. 2.4 Selected IR spectra of $NaNH_2$ collected at room temperature on compression in the spectral regions 500-1700 cm^{-1} (A) and 3150-3400 cm^{-1} (B) in the pressure region 0.05-15.74 GPa. The vertical bar labels the scale of the absolute absorbance intensity. The pressures in GPa are labeled for each spectrum. The assignments are labeled for selected IR modes (see text).

2.3.4. Pressure effects on Raman and IR modes.

The pressure dependences of the observed Raman and IR internal modes of $NaNH_2$ were examined by plotting the vibrational frequencies as a function of pressure as shown in Figs. 2.5 and 2.6. Those for Raman lattice modes are depicted as an inset of Fig. 2.5. The pressure coefficients for these modes are analyzed by least-square fitting of the experimental data and are reported in Table 2.2. In addition to the compelling spectroscopic evidences, possible phase transitions could be further inferred and more accurately located if sharp changes in the pressure coefficients are observed.

In general, all Raman and IR modes exhibited pressure-induced blue shifts, consistent with that the bonds become stiffened upon compression. In the lattice region, all modes can be fitted using linear functions with slopes of almost zero below 1.0 GPa, indicating that the inter-ion interactions within the unit cell are not sensitive to compression in this pressure region. In the region for internal vibrational modes, as can be seen, the distinct changes of pressure dependence as well as the appearance/disappearance of major Raman and IR modes also indicate consistent phase boundaries. In general, the pressure coefficients are the largest in the region below 0.9 GPa, and decrease progressively across the boundaries at around 0.9 and 2.0 GPa. Different pressure dependences are indicative of different compressiblities of different phases. We note that linear regressions can be used for all Raman and IR modes in all pressure regions except for the Raman modes in the region of 0.9-2 GPa, which can be best fit with quadratic functions. The compression behavior of the Raman modes of $NaNH_2$ in this pressure region is similar to that for $LiNH_2$ in a broad pressure region of 0-14 GPa.[23] Overall, the pressure dependences of the major Raman and IR modes collectively indicate several distinct pressure regions in which $NaNH_2$ could exist in different phases. These pressure regions are <0.9 GPa, 0.9-2.0 GPa and >2.0 GPa, which we label as phases I, II and III, respectively.

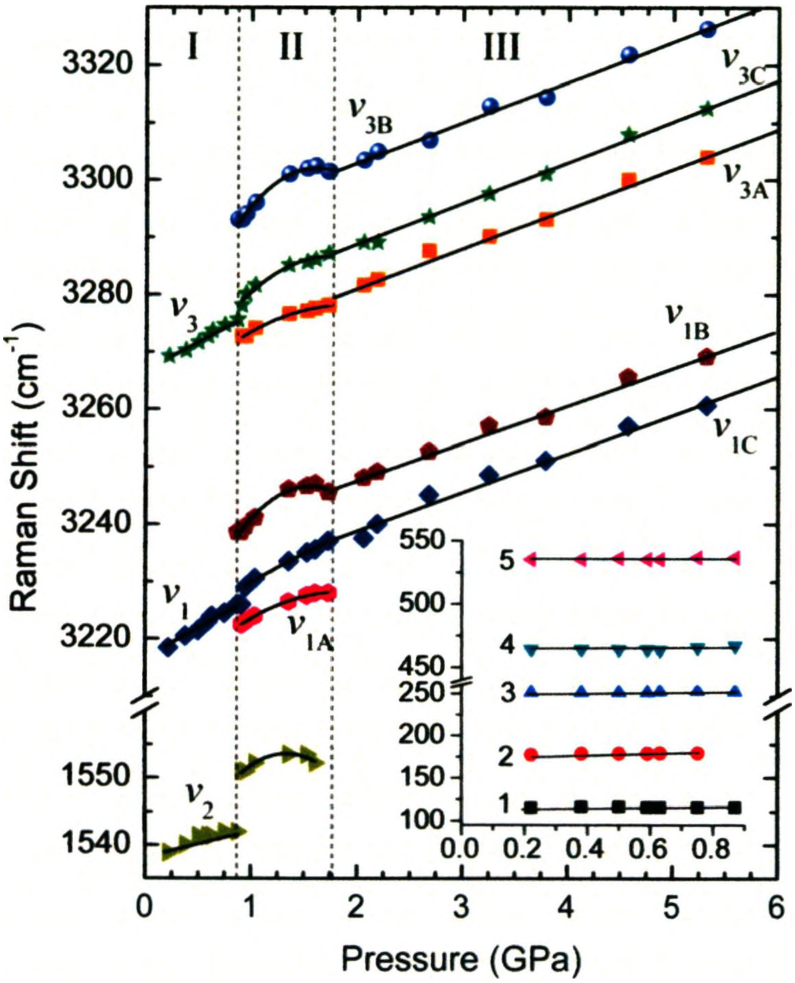

Fig. 2.5 Pressure dependence of Raman modes of $NaNH_2$ on compression. Different symbols represent Raman modes with different origins with assignments labeled (see text). The solid lines crossing the solid symbols are based on linear regressions except for the pressure region of 0.9-2.0 GPa, where quadratic regressions were used for all Raman modes. The vertical dashed lines indicate the proposed phase boundaries.(Inset shows the lattice region)

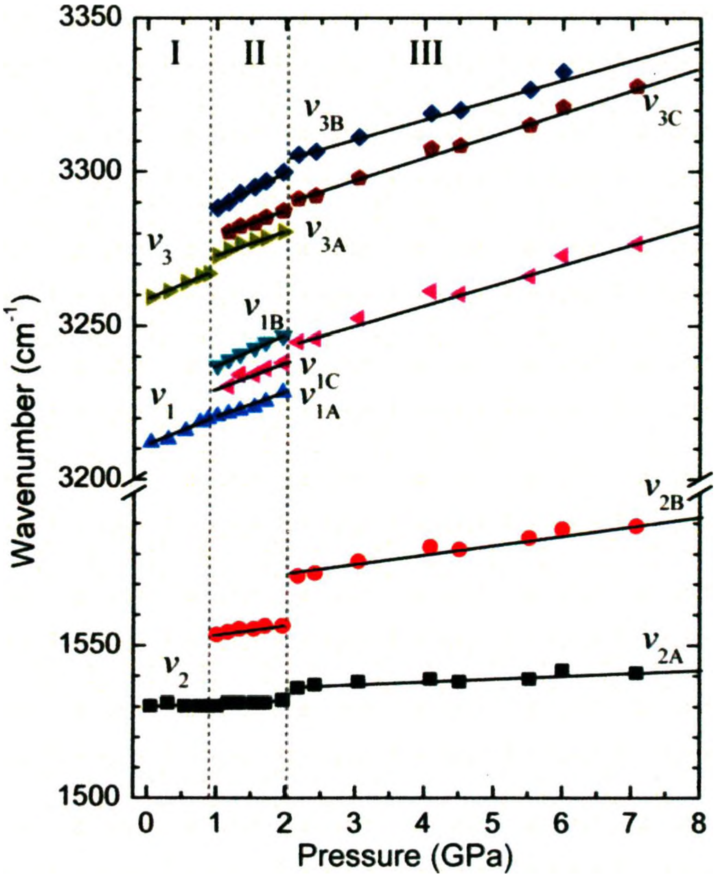

Fig. 2.6 Pressure dependence of IR modes of $NaNH_2$ on compression. Different symbols represent IR modes with different origins with assignments labeled (see text). The solid lines crossing the solid symbols are based on linear regressions. The vertical dashed lines indicate the proposed phase boundaries.

2.3.5. Raman and IR spectra on decompression.

Raman and IR spectra were also collected on decompression all the way down to near-ambient pressure in order to better understand the pressure-induced structural evolutions and the high-pressure stability of $NaNH_2$. During decompression, we observed similar back transformations in both Raman and IR spectra with almost identical transformation pressures as in the compression sequence, indicating very minor or almost negligible hysteresis.

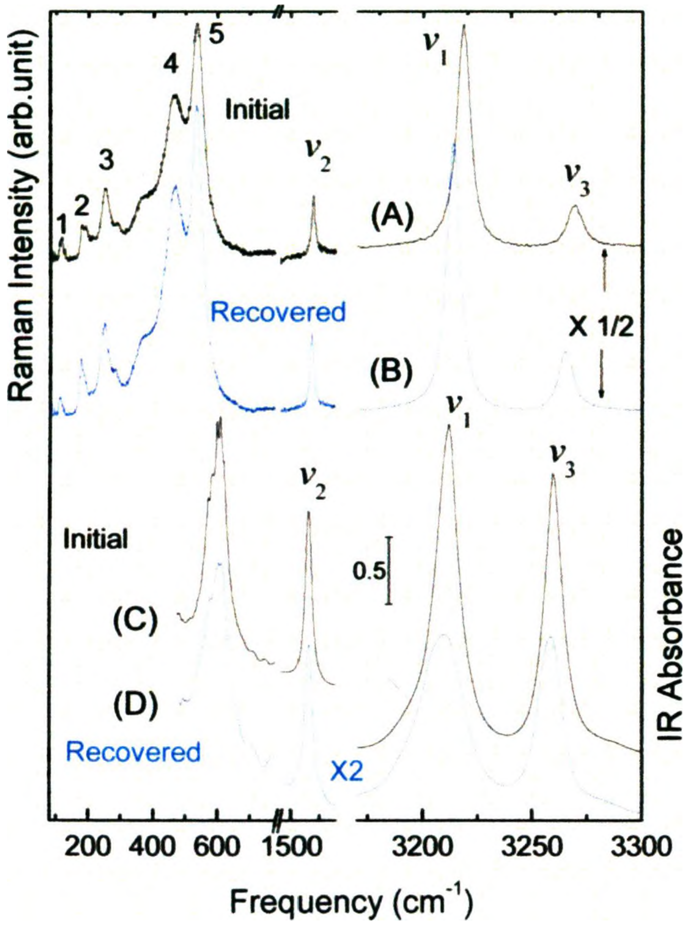

Fig. 2.7 Raman (top) and IR (bottom) spectra of recovered $NaNH_2$ (B and D) upon decompression in comparison with those respective initial near-ambient-pressure spectra before compression (A and C).The Raman intensity is normalized with arbitrary unit labeled along the left vertical axis. The vertical bar indicates the absolute IR absorbance intensity.

More importantly, as can be seen in Fig. 2.7, all fundamental modes, including both internal and lattice modes observed before compression (spectra A and C) at ambient pressure were completely recovered upon decompression to near-ambient pressure (spectra B and D). The difference in Raman shift before and after compression could be due to the different pressures under which the spectra were collected whereas the different IR band shape and band intensity could be associated with the modification of the sample thickness in the compression/decompression cycle. All these observations suggest that the pressure-induced structural transformations of $NaNH_2$ are reversible, and $NaNH_2$ is chemically stable in the entire pressure region in this study.

2.3.6. Discussion.

Our Raman and IR measurements collectively and consistently identified two pressure-induced phase transitions. It is therefore of interest to understand the possible structures of the high pressure phases and thus the nature of the transformations. Phase I (0-0.9 GPa) can be interpreted as the extension of the ambient pressure orthorhombic crystal structure with space group *Fddd* (D_{2h}^{24}) as evidenced by the spectroscopic features in this pressure region. In particular, starting with C_{2v} point group symmetry, the number of vibrational modes and optical activities of NH_2^- can be predicted using factor group analysis as shown in Table 2.3. By identifying the number of molecules per primitive cell (Z=16 and Z'=4 where Z and Z' are number of molecules per unit cell and per primitive cell, respectively), the site symmetry from crystal structure, and the appropriate correlation path, the irreducible representations for the three fundamental frequencies under *Fddd* factor group are

$$\Gamma(\nu_1 \text{ or } \nu_2) = A_g + B_{1g} + A_u + B_{1u} \qquad (1)$$

$$\Gamma(\nu_3) = B_{2g} + B_{3g} + B_{2u} + B_{3u} \qquad (2)$$

Therefore, two Raman active modes (A_g and B_{1g}) and one IR active mode (B_{1u}) are expected for each of ν_1 and ν_2, and two Raman (B_{2g} and B_{3g}) and two IR (B_{2u} and B_{3u}) active modes for ν_3. The observation of only one Raman and one IR active mode in the region of 0-0.9 GPa suggests that the correlation field splitting is not significant enough to be resolved under the current conditions. These comparisons are summarized in Table 2.4.

In the pressure region of 0.9-2.0 GPa, all the three fundamental internal modes in both Raman and IR spectra were found to split into a doublet or a triplet as summarized in Table 2.4, except for the ν_2 mode exhibiting a transient splitting at 0.9 GPa, above which pressure the splitting cannot be obviously identified. These observations suggest that the structure of this phase is characterized by enhanced intermolecular interactions. Since all the internal modes started with the symmetry under which all the vibrations are singly degenerated, the static field splitting can therefore be ruled out as the primary cause. Instead, correlation field splitting due to the interaction of non-equivalent molecules within the same unit cell is most likely the mechanism. If there were no major change of the crystal structure of this phase, doubling of the unit cell content might account for the splitting. However, factor group analysis on the content doubled cell would have predicted quartet or doublet bands, rather than triplets as observed. Therefore, it is highly likely that the crystal structure of phase II is significantly different than phase I, as also suggested by the Raman lattice features in terms of both the number of modes transformation whereas no hysteresis was observed for $NaNH_2$. Most significantly, $LiNH_2$ remained perfectly crystalline even up to 25 GPa with distinctive orientational ordering of NH_2^- ions, in strong contrast to the amorphous/disordering behavior of $NaNH_2$ above 2 GPa. In summary, the significantly different compression behavior of $NaNH_2$ than $LiNH_2$ especially in the low-pressure region may have profound implications in practical applications in that the pressure of a few GPa is more readily achievable by ball milling or other approaches. Nonetheless, additional experimental work on $NaNH_2$ and other amides as well as theoretical investigations are still needed to understand this difference and to further explore amide-based hydrogen storage applications.

Table 2.3 Factor Group Analysis of Vibrational Modes of NH_2^- in Space Group *Fddd* (D_{2h}^{24}).

Mode	Point group C_{2v}	Site symmetry C_2	via C_{2z}	Factor group D_{2h}	Counts	Optical activity [a]
ν_1 ν_2	$2A_1$ (×4)	$2A$ (×4)		A_g	2	R
				B_{1g}	2	R
				A_u	2	-
				B_{1u}	2	IR
ν_3	B_2 (×4)	B (×4)		B_{2g}	1	R
				B_{3g}	1	R
				B_{2u}	1	IR
				B_{3u}	1	IR

[a]. R: Raman active; IR: Infrared active.

Table 2.4 Number of Predicted and Observed Fundamental Vibrational Modes of NH_2^- in Different Phases. [a]

Mode[b]	Predicted	Observed		
	*F*ddd	Phase I	Phase II	Phase III
ν_3 (3269 cm^{-1})	2R + 2IR	1R + 1IR	3R + 3IR	3R + 2IR
ν_1 (3218 cm^{-1})	2R + 1IR	1R + 1IR	3R + 3IR	2R + 1IR
ν_2 (1538 cm^{-1})	2R + 1IR	1R + 1IR	1R + 2IR	2IR

[a] R: Raman active; IR: Infrared active.

[b] The fundamental vibrational modes are listed in decreasing frequency with Raman shifts measured at ambient pressure labeled.

2.4 Conclusions

In situ high-pressure Raman and IR spectroscopic measurements of $NaNH_2$ revealed two pressure-induced phase transitions at around 0.9 and 2.0 GPa. These two transitions are evidenced by both significant changes in spectral profiles and the pressure dependence of Raman and IR modes over different pressure ranges. Upon decompression, all characteristic Raman and IR modes are recovered indicating the pressure-induced transitions are completely reversible. Spectral analysis of the combined Raman and IR data indicates that phase I in the pressure region of ~ 0.9 GPa maintains an orthorhombic structure with a space group *Fddd*, the same as the ambient-pressure structure. In the pressure region of 0.9 - 2.0 GPa (phase II), the structure of $NaNH_2$ may have a completely different crystal lattice likely with a space group of trigonal or hexagonal symmetry. In the pressure region of > 2.0 GPa, the depleted lattice features and broad band profiles in both Raman and IR measurements suggest that phase III is a disordered or amorphous phase. Further experimental and theoretical investigations may help to better understand the structures of newly discovered high-pressure phases.

2.5 Acknowledgements

The authors acknowledge funding support from a Discovery Grant, a Research Tools and Instruments Grant from the Natural Science and Engineering Research Council of Canada, a Leaders Opportunity Fund from the Canadian Foundation for Innovation, an Early Researcher Award from the Ontario Ministry of Research and Innovation and a Petro-Canada Young Innovator Award from the University of Western Ontario.

2.6 References

(1) Schlapbach, L.; Zuttel, A. *Nature* **2001**, *414*, 353.

(2) Grochala, W.; Edwards, P. P. *Chem. Rev. (Washington, DC, U. S.)* **2004**, *104*, 1283.

(3) Vajeeston, P.; Ravindran, P.; Kjekshus, A.; Fjellvag, H. *J. Alloys Compd.* **2005**, *404*, 377.

(4) Goncharov, A. F.; Hemley, R. J. *Chem. Soc. Rev.* **2006**, *35*, 899.

(5) Struzhkin, V. V.; Militzer, B.; Mao, W. L.; Mao, H. K.; Hemley, R. J. *Chem. Rev. (Washington, DC, U. S.)* **2007**, *107*, 4133.

(6) Ravindran, P.; Vajeeston, P.; Fjellvag, H.; Kjekshus, A. *Comp. Mater. Sci.* **2004**, *30*, 349.

(7) Kim, J. H.; Jin, S. A.; Shim, J. H.; Cho, Y. W. *Scr. Mater.* **2008**, *58*, 481.

(8) Xiong, Z. T.; Yong, C. K.; Wu, G. T.; Chen, P.; Shaw, W.; Karkamkar, A.; Autrey, T.; Jones, M. O.; Johnson, S. R.; Edwards, P. P.; David, W. I. F. *Nat. Mater.* **2008**, *7*, 138.

(9) Yang, J. B.; Lamsal, J.; Cai, Q.; James, W. J.; Yelon, W. B. *Appl. Phys. Lett.* **2008**, *92*, 091916.

(10) Lin, Y.; Mao, W. L.; Mao, H. K. *Proc. Natl. Acad. Sci. U. S. A.* **2009**, *106*, 8113.

(11) Sakintuna, B.; Lamari-Darkrim, F.; Hirscher, M. *Int. J. Hydrogen Energy* **2007**, *32*, 1121.

(12) Wu, H. *ChemPhysChem* **2008**, *9*, 2157.

(13) Chen, P.; Xiong, Z. T.; Luo, J. Z.; Lin, J. Y.; Tan, K. L. *Nature* **2002**, *420*, 302.

(14) Janot, R. *Ann. Chim. Sci. Mat.* **2005**, *30*, 505.

(15) Ichikawa, T.; Leng, H. Y.; Isobe, S.; Hanada, N.; Fujii, H. *J. Power Sources* **2006**, *159*, 126.

(16) Xiong, Z. T.; Hu, J. J.; Wu, G. T.; Liu, Y. F.; Chen, P. *Catal. Today* **2007**, *120*, 287.

(17) Zalkin, A.; Templeton, D. H. *J. Phys. Chem.* **1956**, *60*, 821.

(18) Cunningham, P. T.; Maroni, V. A. *J. Chem. Phys.* **1972**, *57*, 1415.

(19) Murli, C.; Song, Y. *J. Phys. Chem. B* **2009**, *113*, 13509.

(20) Song, Y.; Murli, C.; Liu, Z. X. *J. Chem. Phys.* **2009**, *131*, 174506.

(21) Xie, S. T.; Song, Y.; Liu, Z. X. *Can. J. Chem.* **2009**, *87*, 1235.

(22) Liu, A.; Xie, S. T.; Dabiran-Zohoory, S.; Song, Y. *J. Phys. Chem. C* **2010**, *114*, 11635.

(23) Chellappa, R. S.; Chandra, D.; Somayazulu, M.; Gramsch, S. A.; Hemley, R. J. *J.*

Phys. Chem. B **2007**, *111*, 10785.

(24) Mao, H. K.; Xu, J.; Bell, P. M. *J. Geophys. Res. Sol. Ea.* **1986**, *91*, 4673.

(25) Dong, Z. H.; Song, Y. *J. Phys. Chem. C* **2010**, *114*, 1782.

(26) Walrafen, G. E. *J. Chem. Phys.* **1964**, *40*, 3249.

(27) Walrafen, G. E. *J. Chem. Phys.* **1966**, *44*, 1546.

(28) Walrafen, G. E. *J. Chem. Phys.* **1967**, *47*, 114.

(29) Nibler, J. W.; Pimentel, G. C. *Spectrochim. Acta* **1965**, *21*, 877.

(30) Bohger, J. P. O.; Essmann, R. R.; Jacobs, H. *J. Mol. Struct.* **1995**, *348*, 325.

(31) Day, D. H.; Sinclair, R. N. *J. Chem. Phys.* **1971**, *55*, 2807.

Chapter 3 *In situ* high-pressure and low-temperature study of ammonia borane by Raman spectroscopy

A version of this chapter has been submitted to *J. Phys. Chem. C*

3.1 Introduction

As a potential hydrogen storage material, ammonia borane (NH_3BH_3) has received extensive investigations among many solid-state chemical hydrides over the past a few decades.[1-4] Ammonia borane is a lightweight molecular complex with high hydrogen content (19.6 wt %) that exceeds the 2015 U.S. Department of Energy target (9 wt %) for on-board hydrogen storage systems.[5] Consequently, substantial research efforts have been made on the understanding of hydrogen chemistry involving ammonia borane and related B-N compounds.[2,4,6-9] The hydrogen release mechanism has been extensively studied for ammonia borane, and it was found the three thermolysis steps require different high temperatures and exhibit very slow kinetics.[2-3] Therefore, the hydrogen storage application using ammonia borane and its derivatives has been examined with extended materials and conditions. For instance, a class of composition modified ammonia borane derivatives, such as alkali-metal amidoboranes, was found to release hydrogen at relatively lower temperatures.[8-10] More recently, Li et al. showed that hydrogen can be released from ammonia borane confined in the metal-organic framework with enhanced kinetics and at lower temperatures (e.g., ~ 30 °C).[7]

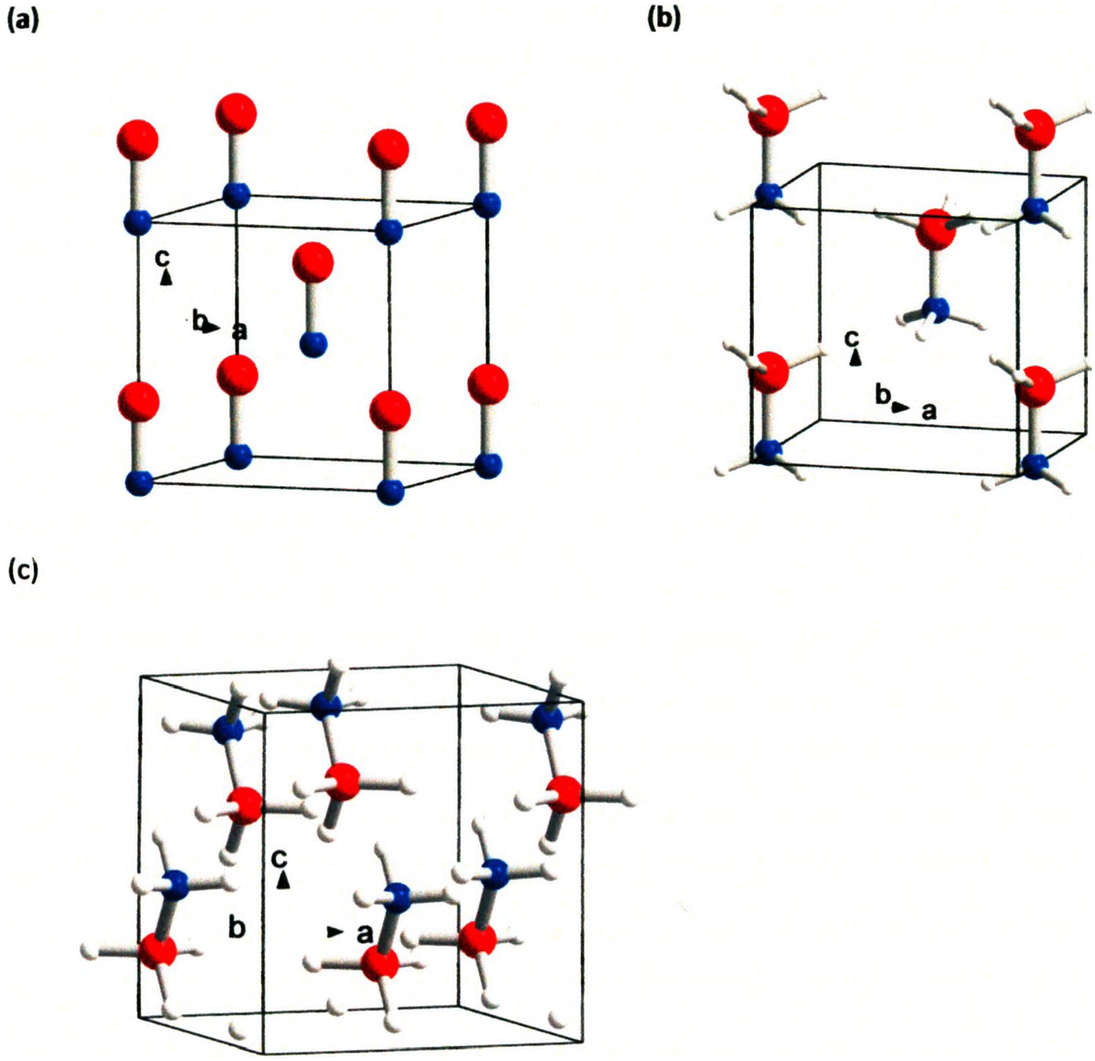

Fig. 3.1 Known crystal structures of NH_3BH_3 (a) at ambient pressure and room temperature, tetragonal structure (space group *I4mm*), (b) at ambient pressure and 225 K, orthorhombic structure (space group $Pmn2_1$), (c) above 1.5 GPa and room temperature, orthorhombic structure (space group $Cmc2_1$). (See Ref Chen & Filinchuk). The coordinate system is indicated to show the orientations of the unit cell.

The structures of ammonia borane have been studied by X-ray diffraction, neutron diffraction and theoretical calculations under ambient conditions or at low temperatures.[10-19] At ambient conditions, ammonia borane adopts the disordered bodycentered tetragonal structure (space group *I*4mm with two molecules per unit cell, Fig. 3.1 a) with cell parameters a= 5.255Å , c= 5.048 Å.[17] At low temperatures, an ordered orthorhombic structure (space group *Pmn*2_1 with two molecules per unit cell, Fig. 3.1 b) with cell parameters a= 5.517 Å, b= 4.742 Å and c= 5.020 Å was identified by Bowden et al.[16] using X-ray diffraction at 90 K, and by Klooster et al. [18] using single crystal neutron diffraction at 200 K. In their studies, the unconventional dihydrogen bonding was reinforced due to the strong dipole-dipole intermolecular interactions and short distances between hydrogen atoms with N-H being the proton donor and H-B the proton acceptor. [16,18]

The application of high-pressure to materials may induce significant changes in molecular structures and associated properties, such as enhanced hydrogen storage capacities, and therefore, a wide range of hydride complexes (e.g., ammonia borane, diborane, calcium borohydride and sodium amide) as potential hydrogen storage materials have been investigated under high pressures.[20-24] Using vibrational spectroscopy, X-ray diffraction and neutron diffraction as well as *ab initio* calculations, ammonia borane, in particular has been extensively studied under high pressure conditions as well.[24-31] Early spectroscopy studies demonstrated that NH_3BH_3 undergoes two phase transitions upon compression to 40 kbar.[25-26] Later, Lin et al. [27] and Xie et al. [24] performed independent high-pressure studies on ammonia borane up to 20 GPa using Raman spectroscopic and combined Raman/IR spectroscopy respectively, and found similar new phase transitions were found in the higher pressure regions. The crystal structures of these new high-pressure phases were subsequently examined by X-ray diffraction measurements and theoretical calculations by Filinchuk et al.[28] and

Chen et al.[29] They consistently established that at room temperature and above 1.5 GPa, NH_3BH_3 crystallizes into a new ordered orthorhombic structure (space group $Cmc2_1$ with four molecules per unit cell, Fig. 3.1 c). Further high-pressure X-ray and neutron diffraction experiments and density functional theoretical calculations confirmed these observations, but also proposed a new triclinic structure with space group $P1$ above 8 GPa.[30] Most recently, Wang et al.[31] investigated the structural and dynamical properties of ammonia borane at high pressure phases up to 60 GPa by molecular dynamics simulations, which helped with the understanding of relationship and the transformation mechanism among the three known phases of ammonia borane.

Furthermore, pressure-induced formation of novel hydrogen containing complexes has demonstrated strong promise in the development of new hydrogen storage materials.[32-37] Especially for ammonia borane, for instance, the significant abundance of stored molecular hydrogen (8-12 wt % H_2) in the ammonia borane – hydrogen complexes [$NH_3BH_3{\cdot}(H_2)_x$] formed under high pressure shows great potential for using ammonia borane as a possible hydrogen storage material.[33-34,36] For practical applications, it would be desirable to recover the hydrogen complexes at near ambient conditions. Indeed, a previous high-pressure study on hydrogen clathrate hydrate formed under high pressures indicated that the complex can be quenched to ambient pressure, but only at low temperatures (e.g., < 145 K).[35] Therefore, it is of great interest to explore the structures and properties of ammonia borane in wider P-T range, especially in the low-temperature region, as well as the reversibility of pressure-induced structural changes at low temperatures. Temperature induced phase transitions have been observed previously using Raman spectroscopy, but only at ambient pressure.[19] Here we report the first *in situ* simultaneous high-pressure and low-temperature experiments on ammonia borane by Raman spectroscopy up to 15 GPa and down to 80 K. We found interesting, new P-T induced transformations and these observations allow a more in-depth understanding of the structures and properties of ammonia borane that are important for hydrogen storage applications.

3.2 Experimental Section

3.2.1 Sample preparation

White ammonia borane powders (97%) were purchased from Sigma-Aldrich and used without further purification. The identity and purity were confirmed by comparing the observed Raman spectrum with that from the reference.[24] A symmetric diamond anvil cell (DAC) equipped with a pair of type-I diamonds with 300 μm culets was used for the high-pressure experiments. This DAC made of BeCu, was specially designed to allow use in a cryostat for *in situ* low-temperature measurements. A tungsten gasket was pre-indented to 50 μm thick and a hole with 100 μm diameter was drilled at the center as the sample chamber. The sample was loaded into the DAC in a MBraun LABmaster glovebox to accommodate the hygroscopicity of the sample. The nitrogen atmosphere in the glovebox was maintained with < 10 ppm H_2O and O_2 during loading of the sample. For the same reason, no fluid pressure transmitting medium was used. A few ruby chips were placed inside the sample chamber as the pressure calibrant. To calibrate the temperature effects on ruby fluorescence lines, we loaded additional ruby chips outside the sample chamber on the back surface of the diamond as the ambient-pressure reference. The pressure was determined using the R_1 fluorescence line by fitting the simultaneous pressure and temperature dependence that was established previously by Ragan et al.[38]

and Yen et al.[39] The ruby spectral profiles showed no significant non-hydrostatic effects particularly in the lower pressure regions (e.g. < 10 GPa) at low temperatures.

3.2.2 High-pressure and low-temperature Raman measurements

To achieve simultaneous high-pressure and low-temperature conditions, we used a customized cryogenic station designed and constructed by Cryo Industries Inc. The cryostat contains a compact vacuum chamber that houses the DAC anchored by a cold collar. A vacuum of 1×10^{-7} torr was maintained in the cryostat chamber by a turbo pump to ensure thermal insulation between the sample and environment. Liquid nitrogen as the cryogen was introduced via an internal loop through the cold collar to allow effective cooling of the DAC conductively down to 77 K. Two silicon dioxide sensors were placed in different locations: one on the cold collar and one on the diamond seat (made of tungsten carbide). The temperature was measured and controlled by a Cryo-con temperature controller from Cryogenic Control System Inc. with an accuracy of ± 1 K. The temperature readings from the two sensors suggest a maximum temperature gradient of 1 K. The cryostat is equipped with two panels with different optical windows. For Raman measurements, the front window material is fused silica, while the back window can be any transparent material for illumination purpose. In addition, the back panel has a feedthrough housing four retractable hex-keys that can be engaged with the screws on the DAC inside the cryostat. Twisting these keys will allow the change of pressure at low-temperatures *in situ*.

Raman measurements were carried out with a customized Raman microspectroscopy system accommodating the operation of the cryostat. A 488 nm blue laser produced by Innova Ar^+ laser (Coherent Inc.) as the excitation source was focused on the sample through the optical windows on the front panel of the cryostat by a 10× Mitutoyo objective. The scattered Raman light was dispersed by a SpectroPro spectrometer, and collected by a liquid-nitrogen-cooled charge-coupled device (CCD) detector, both from Acton. Rayleigh scattering was removed by a pair of notch filters that enabled a spectral range >100 cm^{-1} to be measured. A grating with 1800 lines/mm was used achieving a resolution of 0.1 cm^{-1}. Neon lines were used for the spectral calibration of the system with an uncertainty of ± 1 cm^{-1}.

3.2.3 Pressure-Temperature (P-T) path design

In the experiments, we designed different P-T paths each with multiple runs to ensure the reproducibility. Initially, we examined the temperature effects by cooling the sample from room temperature to 80 K at ambient pressure as well as at the highest pressure, 15.94 GPa. Then, to investigate the pressure effects at low temperatures, we compressed the sample up to 15.94 GPa isothermally at 180 K. Finally, we performed decompression and warming up procedures to check the reversibility of the transformations.

3.3 Results and Discussion

Raman spectra of ammonia borane were collected under ambient conditions as a starting point and are shown at the bottom of Fig. 3.2. At ambient pressure and temperature, ammonia borane has a C_{3v} molecular symmetry and C_{4v} factor group symmetry (for space group *I4mm*). Thus the irreducible representation for Raman active modes are[19]:

$$\Gamma^{I4mm}_{\text{internal}} = 5A_1 + 6E \tag{1}$$

$$\Gamma^{I4mm}_{\text{lattice}} = E \tag{2}$$

where the A_2 mode is omitted from the above representations since it is not Raman active. Therefore, the assignment of the observed Raman modes can be made by adopting the previous work[19,24] as shown in Table 3.1.

Table 3.1 Assignments and Vibrational Frequencies (cm^{-1}) of Observed Raman Modes of NH_3BH_3 at Ambient Pressure and Different Temperatures

This work		Reference[a]			Description
Room T	180 K	298K	224 K	88 K	
3314 ν_7(E)	3327 ν_{7a}	3316	3327	3338	Asym. N-H stretch
				3331	
	3292 ν_{7b}		3302	3300	
				3290	
3250 $\nu_1(A_1)$	3246 ν_1	3250	3249	3247	Sym. N-H stretch
				3240	
3172	3198	3176	3199	3202	overtone?
	3161		3171	3165	
	2439 ν_{8c}		2413	2434	
				2400	
2375 ν_8(E)	2386 ν_{8a}	2375	2371	2373	Asym. B-H stretch
	2356 ν_{8b}			2356	
			2340	2343	
2278 $\nu_2(A_1)$	2295 ν_{2a}	2279	2280	2289	Sym. B-H stretch
	2271 ν_{2b}		2263	2263	
	1620 ν_{9d}		1615	1622	NH_3 deformation
	1606 ν_{9c}			1609	
1596 ν_9(E)	1592 ν_{9a}	1600	1595	1593	
	1582 ν_{9b}			1585	

1189	1217	ν_{10a}	1189	1209	1214	BH_3 deformation
$\nu_{10}(E)$						
	1186	ν_{10d}		1178	1180	
	1179	ν_{10c}			1173	
	1170	ν_{10b}		1164	1166	
1158	1162	ν_{4a}	1155	1156	1157	BH_3 deformation
$\nu_4(A_1)$						
				1080	1086	
1067	1073	ν_{11b}	1065	1066	1073	NBH rock
$\nu_{11}(E)$						
	1058	ν_{11a}		1062	1056	
799	820	ν_5'	800	804	813	
$\nu_5'(A_1)$						^{10}B-N stretch
					810	
					798	
784	804	ν_5	784	789	794	^{11}B-N stretch
$\nu_5(A_1)$						
728	743	ν_{12a}	727	734	740	NBH rock
$\nu_{12}(E)$						
	733	ν_{12c}		727	731	
	722	ν_{12b}		723	721	
124 L	212	L_2	–	–	–	Lattice mode
	94	L_1				

a. Reference 19.

Fig. 3.2

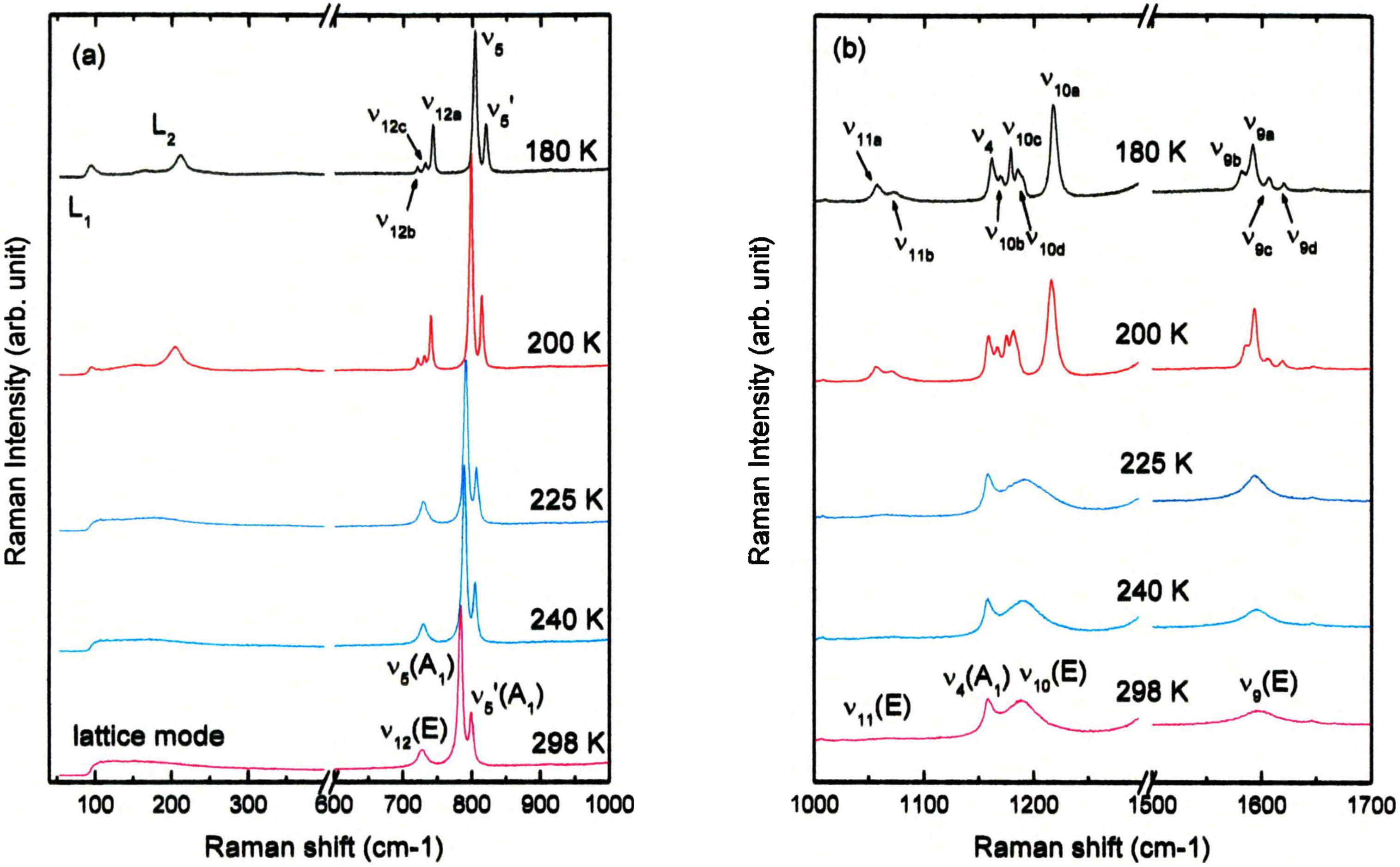
(a)
L2
L1
ν12c
ν12a
ν5
ν5'
ν12b
180 K
200 K
225 K
240 K
ν5(A1)
ν5'(A1)
lattice mode
ν12(E)
298 K
Raman Intensity (arb. unit)
100
200
300
600
700
800
900
1000
Raman shift (cm-1)
(b)
ν10a
ν11a
ν4
ν10c
ν9b
ν9a
ν11b
ν10b
ν10d
ν9c
ν9d
180 K
200 K
225 K
240 K
298 K
ν11(E)
ν4(A1)
ν10(E)
ν9(E)
Raman Intensity (arb. unit)
1000
1100
1200
1500
1600
1700
Raman shift (cm-1)

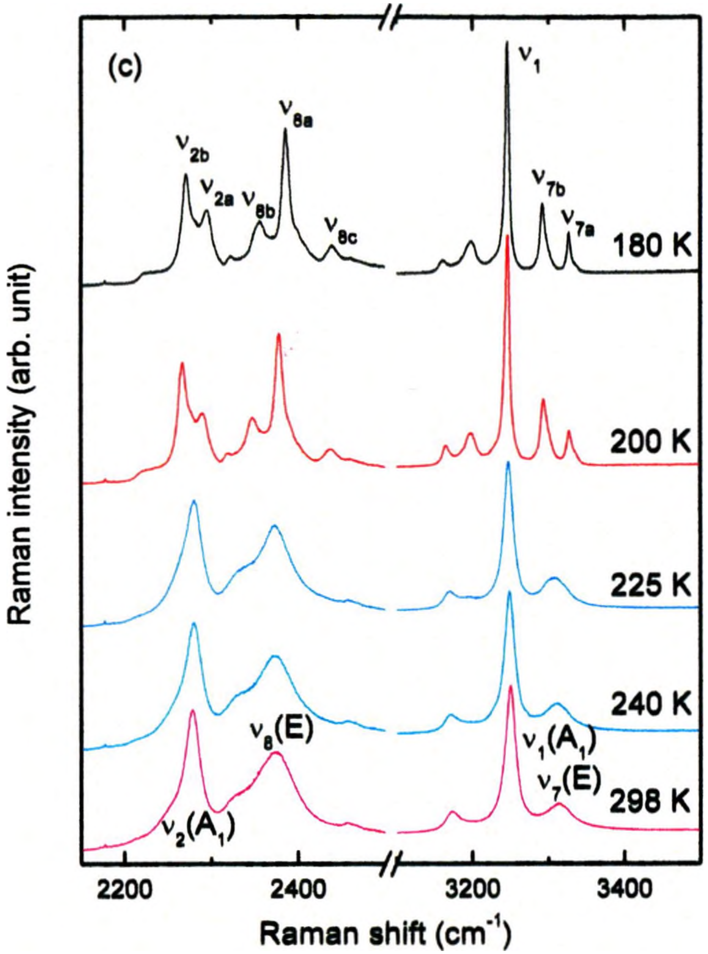

Fig. 3.2 Selected Raman spectra of NH_3BH_3 collected at ambient pressure from 298 to 180 K in the region of 50-1000 cm^{-1} (a), 1000-1700 cm^{-1} (b) and 2150-3500 cm^{-1} (c).

The relative intensities are normalized and thus are directly comparable. The temperatures are labeled for each spectrum. The assignments are labeled for each Raman mode at 298 K and 180 K (see Table 3.1).

3.3.1 Raman spectra during cooling down to 180 K

Raman spectra were collected as a function of temperature from 298 K to 180 K at near ambient pressure. Selected Raman spectra from the cooling sequence are depicted in Fig. 3.2. Significant sharpening of the lattice modes as well as characteristic splitting of internal modes with *E* symmetry were observed when the temperature was lowered to < 220 K. For example, two new lattice modes (L_1 and L_2) appeared at 94 and 212 cm^{-1}, which became much sharper and more pronounced, indicating the transition into a new crystal structure. In addition, the doubly degenerate modes (e.g., the NBH rocking mode v_{12} and $v_{11,}$ the BH_3 deformation mode v_{10}, the NH_3 deformation mode v_9, the asymmetric B-H stretching mode v_8, and the asymmetric N-H stretching mode v_7) all split into two to four components (Fig. 3.2 and Table 3.1). Notably, low temperature (220 K) also induced splitting in the symmetric B-H stretching mode, $v_2(A_1)$. These obvious changes collectively suggest a phase transition below 225 K, consistent with the previous observations by Hess et al.[19] The labeling of the new components of the Raman modes as a result of splitting at low temperatures follows the convention, the original and the most prominent peak is assigned as v_a, whereas all the other affiliated components are assigned based on their appearing sequence (e.g., as v_b, v_c, v_d, etc.).

3.3.2 Raman spectra on compression to 15.92 GPa at 180 K

3.3.2.1 Lattice region. (Fig. 3.3 a). Upon compression to 1.5 GPa, three new lattice modes (labeled as L_3, L_4 and L_5) were observed with concurrent vanishing of the two original lattice modes L_1 and L_2. This observation, together with the very sharp and intense new lattice mode L_4 at 178 cm^{-1}, indicated a major phase transition into a new ordered crystal structure. This new phase spans in the pressure region of 1.5-5.0 GPa as suggested by the similar Raman profiles in this region. Above 5.0 GPa, the L_3 and L_5 modes gradually diminished, and completely vanished above 8.0 GPa. Concurrently, a significant band broadening was observed above 8.0 GPa, suggesting another phase transition, possibly to a more disordered structure. Compared with the previous high-pressure studies of ammonia borane at room temperature,[24] the Raman profiles observed here are quite similar, except that more lattice modes were observed in the lower pressure region (i.e.,1.5-5.0 GPa) but less in the higher pressure regions (i.e., > 5.0 GPa).

3.3.2.2 NBH rocking regions. (Fig. 3.3 b and Fig. 3.3 c). There are two NBH rocking modes: the low-frequency mode ν_{12} (700-850 cm^{-1}) and high-frequency mode ν_{11} (1025-1150 cm^{-1}). The change of the ν_{12} mode from a triplet to a new blue-shifted doublet, together with the abrupt change of Raman shift and the broadening of the ν_{11} modes, strongly suggest a phase transition at 1.5 GPa. Upon further compression, the disappearance of the doublet ν_{12} mode and the gradual development of the ν_{11} mode into a prominent triplet at 5.0 GPa clearly signified another phase transition at this pressure. When compressed to above 8.0 GPa, the ν_{12} mode totally faded away while there was a dramatic reduction in the intensities of ν_{11} modes, implying a third phase transformation, as consistently indicated by the lattice profiles.

3.3.2.3 BH_3 and NH_3 deformation regions. (Fig. 3.3 c and Fig. 3.3 d). There are two BH_3 deformation modes in the region of 1100-1300 cm^{-1}, i.e., ν_4 and ν_{10} modes, and one degenerate NH_3 deformation mode, ν_9, in the region of 1500-1650 cm^{-1}. As the pressure was increased above 1.5 GPa, the ν_{10} mode was strongly perturbed: it first red-shifted abruptly by -23 cm^{-1} and subsequently developed into a doublet at 2.74 GPa. In contrast, the ν_9 mode exhibited a blue shift and merged from a quartet into a doublet. This evidence suggests a phase transformation at 1.5 GPa as indicated by the other modes. The ν_{10a} mode exhibited another abrupt red shift above 5.0 GPa, at which pressure the intensity of the two components of the ν_9 mode switched. Beyond 8.0 GPa, the ν_{10} modes split into a triplet, whereas the ν_4 mode is almost indiscernible. All of these observations corroborate two additional phase changes at 5.0 GPa and 8.0 GPa respectively.

3.3.2.4 B-H and N-H stretching regions. (Fig. 3.3 e and 3.3 f). The Raman features in the stretching regions resemble the other regions described above. In particular, the multiple components of the symmetric B-H stretching ν_2 mode merged into a single prominent band, while the asymmetric B-H (N-H) stretching mode ν_8 (ν_7) evolved from triplet (doublet) into new convoluted patterns at 1.5 GPa. Above 5.0 GPa, the doublet ν_7 mode further merged into a single mode, consistent with the proposed second phase transition. Furthermore, the significant merging of *all* the ν_8 components suggests the third phase transition above 8.0 GPa.

Fig. 3.3

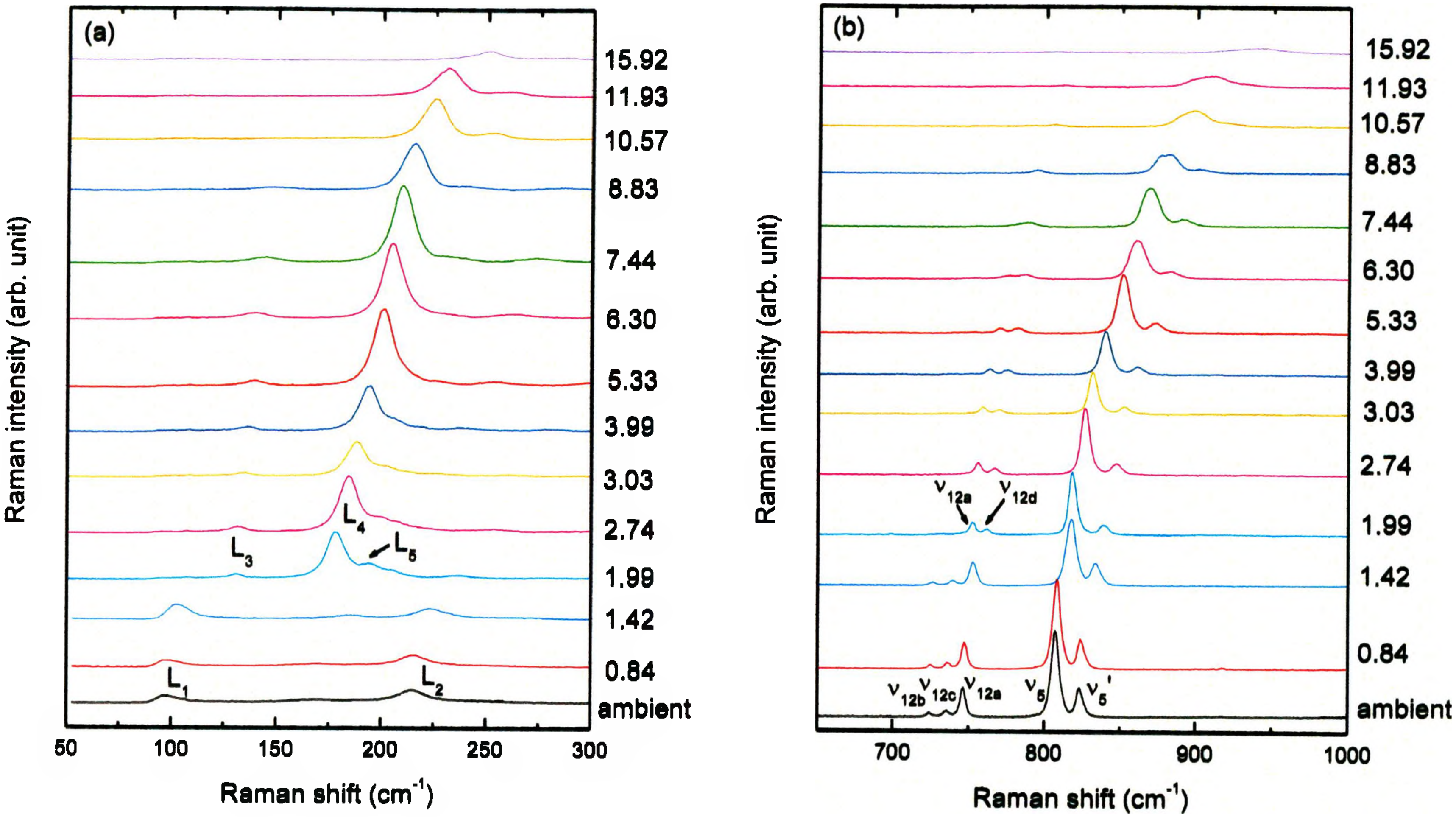
(a)
15.92
11.93
10.57
8.83
7.44
6.30
5.33
3.99
3.03
2.74
1.99
1.42
0.84
ambient
L_1
L_2
L_3
L_4
L_5
Raman intensity (arb. unit)
50
100
150
200
250
300
Raman shift (cm^{-1})
(b)
15.92
11.93
10.57
8.83
7.44
6.30
5.33
3.99
3.03
2.74
1.99
1.42
0.84
ambient
ν_{12a}
ν_{12d}
ν_{12b}
ν_{12c}
ν_{12a}
ν_5
ν_5'
Raman intensity (arb. unit)
700
800
900
1000
Raman shift (cm^{-1})

Fig. 3.3

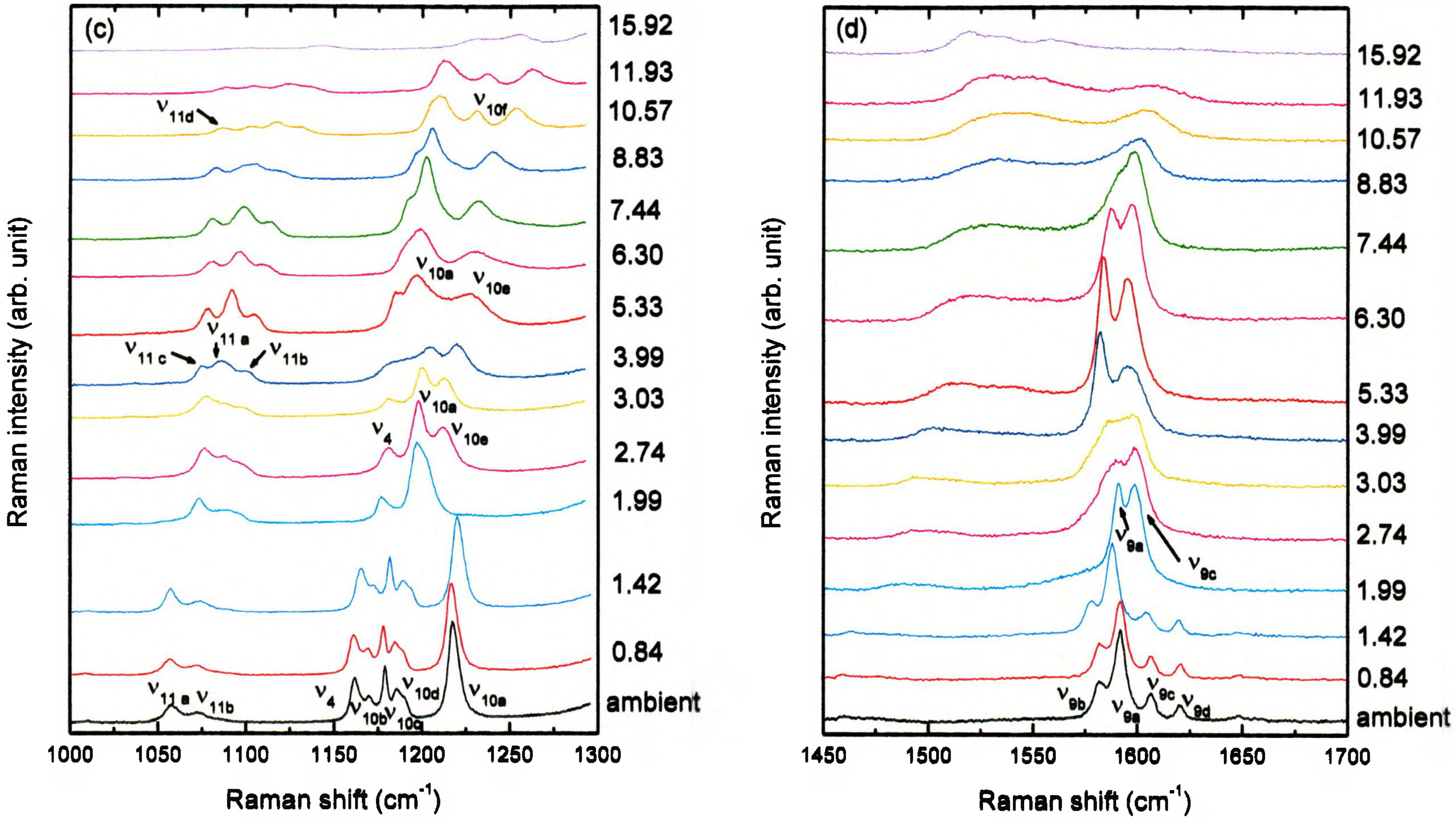
(c)
Raman intensity (arb. unit)
Raman shift (cm^{-1})
1000
1050
1100
1150
1200
1250
1300
15.92
11.93
10.57
8.83
7.44
6.30
5.33
3.99
3.03
2.74
1.99
1.42
0.84
ambient
ν_{11d}
ν_{10f}
ν_{10a}
ν_{10e}
ν_{11c}
ν_{11a}
ν_{11b}
ν_{10a}
ν_{4}
ν_{10e}
ν_{11a} ν_{11b}
ν_{4}
ν_{10b}
ν_{10c}
ν_{10d}
ν_{10a}
(d)
Raman intensity (arb. unit)
Raman shift (cm^{-1})
1450
1500
1550
1600
1650
1700
15.92
11.93
10.57
8.83
7.44
6.30
5.33
3.99
3.03
2.74
1.99
1.42
0.84
ambient
ν_{9a}
ν_{9c}
ν_{9b}
ν_{9a}
ν_{9c}
ν_{9d}

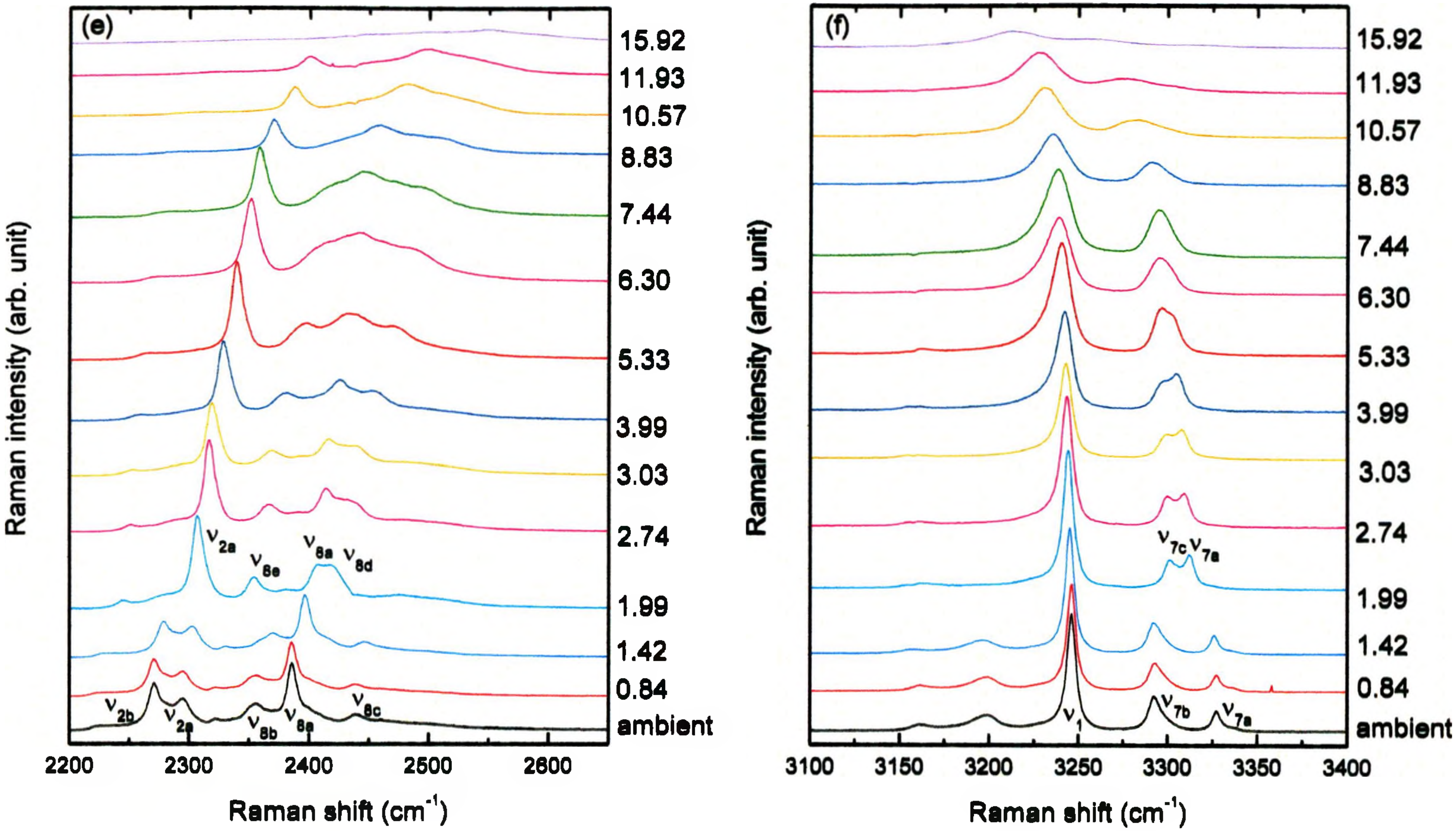

Fig. 3.3 Selected Raman spectra of NH_3BH_3 collected on compression up to 15.92 GPa at 180 K in the region of 50-3400 cm^{-1} (a,b,c,d,e,f). The relative intensities are normalized and thus are directly comparable. The units of the pressures are in GPa for each spectrum. The assignments are labeled for selected Raman mode at selected pressures (see Table 3.1).

3.3.3 Pressure effects on Raman modes

The phase transition boundaries suggested by the Raman features described above can be better visualized by examining the pressure dependences of the characteristic Raman modes (as shown in Fig. 3.4). Pressure coefficients (*dv/dP*) were calculated by fitting quadratic (< 1.5 GPa) or linear (1.5-15.94 GPa) regressions of the original experimental data. As can be seen in Figure 3.4, four distinct pressure regions with possibly different phases can be inferred by the sharp changes in the pressure dependence. These pressure coefficients are larger in the second (1.5-5.0 GPa) and fourth (> 8.0 GPa) phases while they are relatively smaller in the other two phases (i.e., < 1.5 GPa and 5.0-8.0 GPa), indicating different compressibilities of these phases. Generally speaking, most of the Raman modes displayed the pressure-induced blue shifts due to the stiffening of most bonds of ammonia borane. However, the N-H stretching modes, such as ν_7 and ν_1 modes, have conspicuously negative slopes (e.g., -1.39, -0.71 and -4.81 cm^{-1} GPa^{-1} for the ν_7 mode in the three high pressure regions, respectively). More interestingly, both components of the ν_9 mode exhibited a change of the sign of the pressure coefficient, from negative to positive across the phase boundary at 5 GPa. The soft behavior of these Raman modes could be explained by weakening of the N-H bond and strengthening of the dihydrogen bond by compression.[24,27,31] All of these observations are consistent with our previous high-pressure Raman measurements on ammonia borane at room temperature.[24]

Fig. 3.4

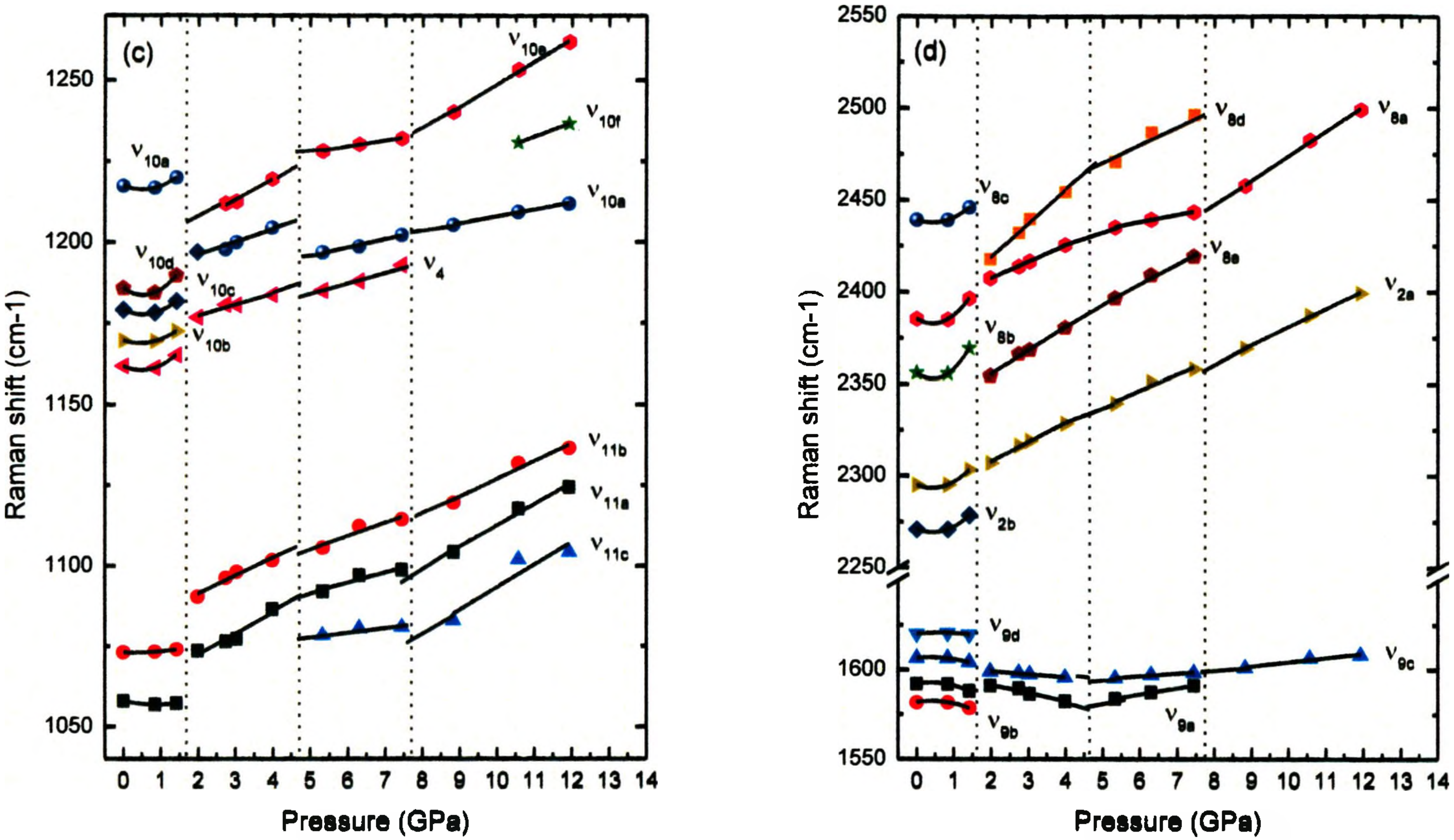
(c)
ν_{10e}
ν_{10f}
ν_{10a}
ν_{10a}
ν_{10d}
ν_{10c}
ν_{10b}
ν_4
ν_{11b}
ν_{11a}
ν_{11c}
Raman shift (cm-1)
1050
1100
1150
1200
1250
0 1 2 3 4 5 6 7 8 9 10 11 12 13 14
Pressure (GPa)
(d)
ν_{8c}
ν_{8d}
ν_{8a}
ν_{8e}
ν_{8b}
ν_{2a}
ν_{2b}
ν_{9d}
ν_{9c}
ν_{9b}
ν_{9a}
Raman shift (cm-1)
1550
1600
2250
2300
2350
2400
2450
2500
2550
0 1 2 3 4 5 6 7 8 9 10 11 12 13 14
Pressure (GPa)

Fig. 3.4

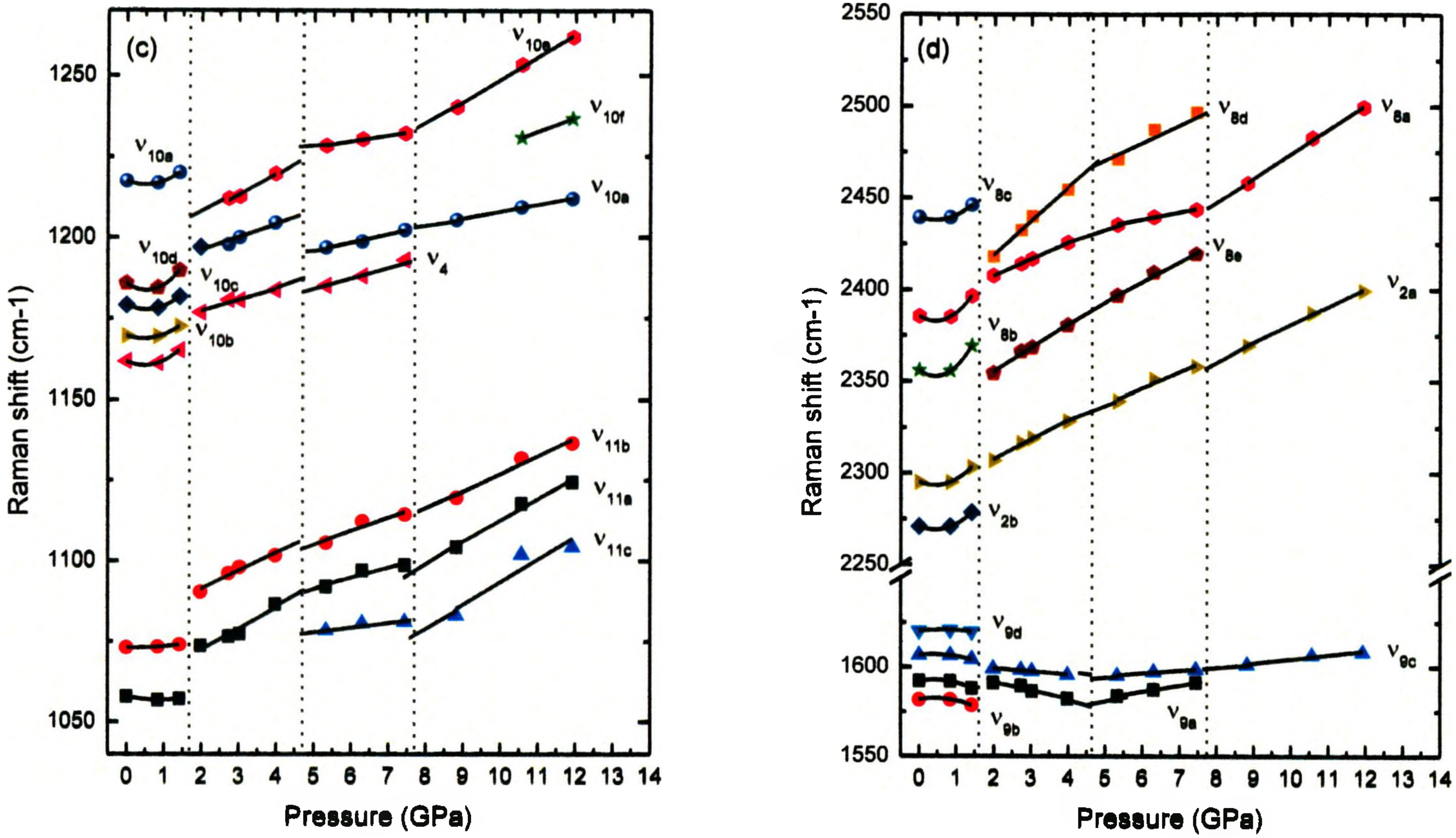
(c)
Raman shift (cm-1)
Pressure (GPa)
1050
1100
1150
1200
1250
0 1 2 3 4 5 6 7 8 9 10 11 12 13 14
ν10a
ν10d
ν10c
ν10b
ν10e
ν10f
ν4
ν11b
ν11a
ν11c
(d)
Raman shift (cm-1)
Pressure (GPa)
1550
1600
2250
2300
2350
2400
2450
2500
2550
0 1 2 3 4 5 6 7 8 9 10 11 12 13 14
ν8c
ν8d
ν8a
ν8e
ν8b
ν2a
ν2b
ν9d
ν9c
ν9b
ν9a

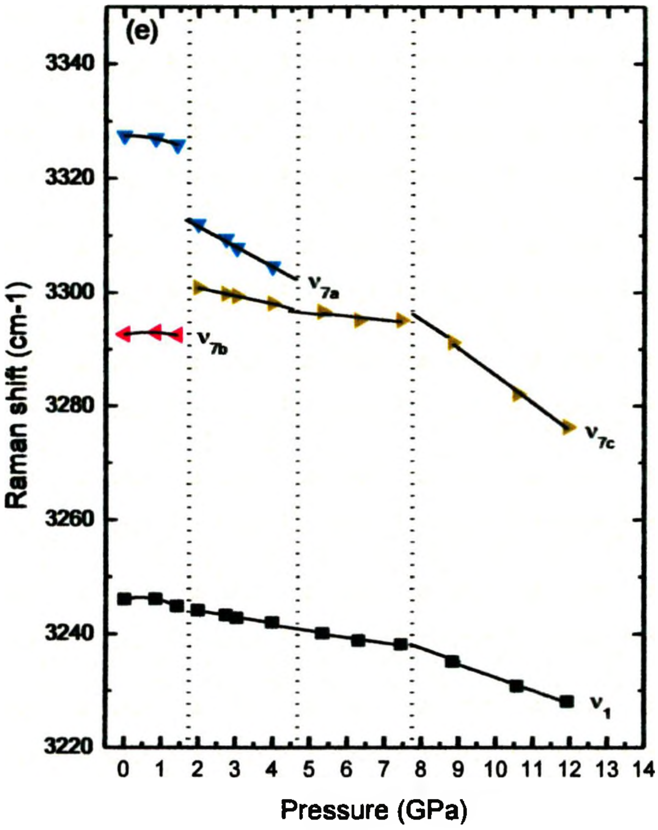

Fig. 3.4 Pressure dependence of Raman modes of NH_3BH_3 on compression at 180 K. Different symbols represent Raman modes with different origins. The solid lines crossing the solid symbols are based on linear regression. The vertical dashed lines indicate the proposed phase boundaries.

3.3.4 Raman spectra upon decompression and warming up

To better understand the combined low-temperature and high-pressure effects on ammonia borane as well as the reversibilities of the observed transitions, the experiments were carried out by decompression and warming up as well. However, it is difficult to strictly follow an isobaric or an isothermal path due to the correlation of the pressure and temperature, a mechanical response from the cell. As a result, after achieving the lowest temperature 80 K and highest pressure 15.94 GPa, Raman measurements were collected on simultaneous decompression and warming up, with selected spectra shown as they were in Fig. 3.5. At 3.43 GPa and 165 K, for instance, both the lattice modes and other internal modes were recovered to resemble the initial pattern at 180 K and 1.5 GPa in the same phase region. Similarly, the Raman pattern observed at 1.21 GPa and 220 K upon decompression and warming up is almost identical to the initial spectrum taken at similar P-T conditions. Therefore, all the phase transitions are reversible with very little hysteresis upon decompression and warming up.

Fig. 3.5

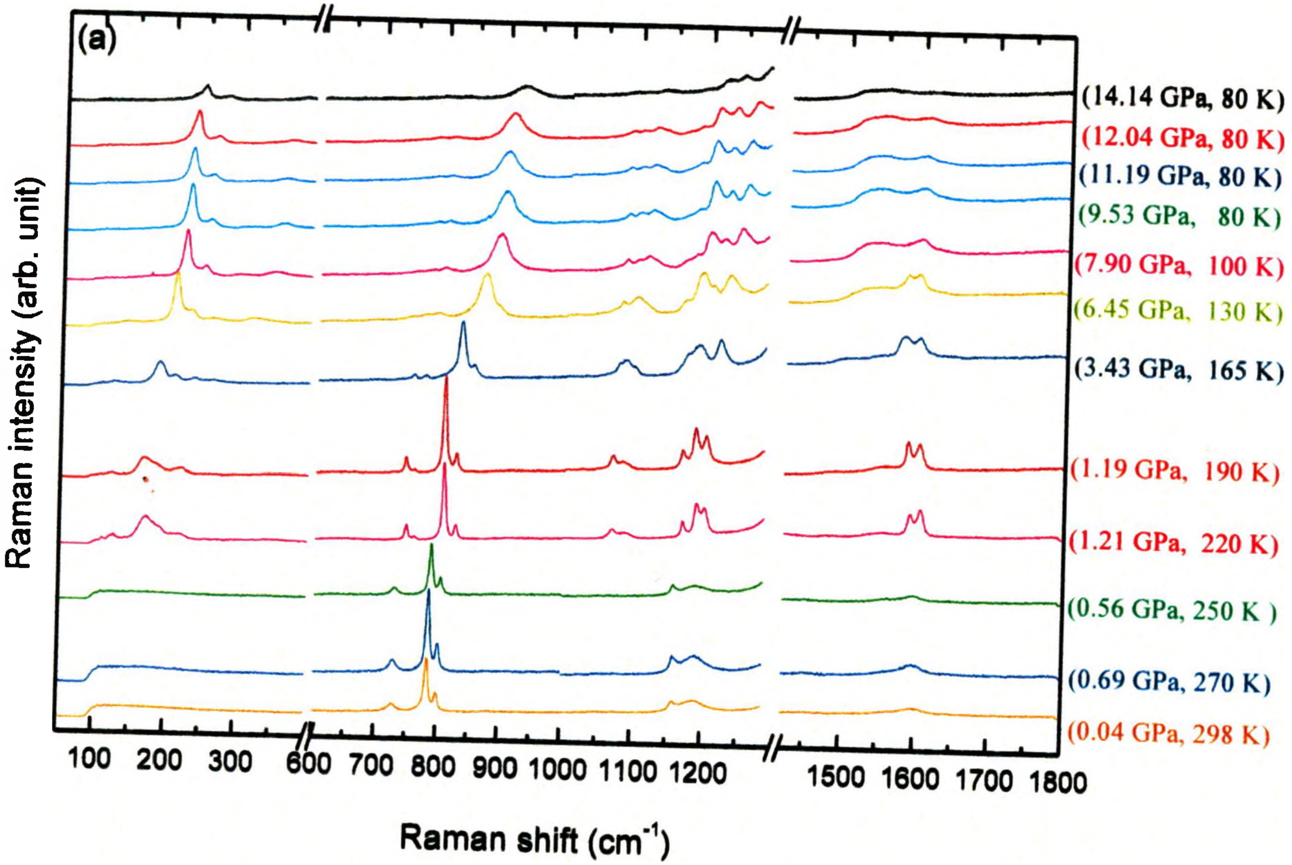
(a)
Raman intensity (arb. unit)
Raman shift (cm^{-1})
100
200
300
600
700
800
900
1000
1100
1200
1500
1600
1700
1800
(14.14 GPa, 80 K)
(12.04 GPa, 80 K)
(11.19 GPa, 80 K)
(9.53 GPa, 80 K)
(7.90 GPa, 100 K)
(6.45 GPa, 130 K)
(3.43 GPa, 165 K)
(1.19 GPa, 190 K)
(1.21 GPa, 220 K)
(0.56 GPa, 250 K)
(0.69 GPa, 270 K)
(0.04 GPa, 298 K)

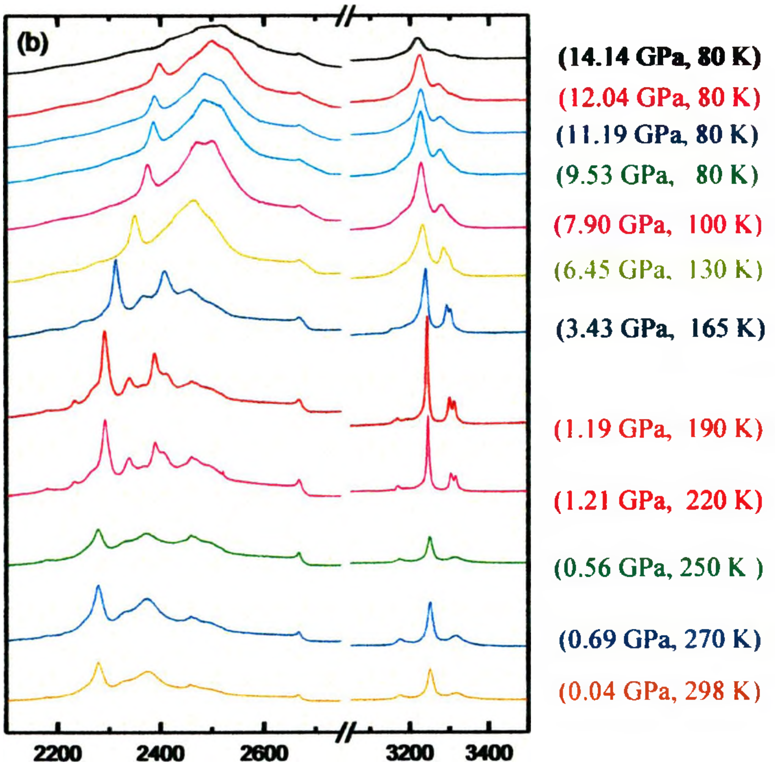

Fig. 3.5 Selected Raman spectra during decompression and warming up processes from 14.14 GPa, 80 K to ambient pressure, room temperature in the spectral region of 100-3400 cm^{-1} (Fig. 3.5 a and 3.5 b). The (P, T) is labeled for each spectrum in the experimental sequence starting from the top and ending at the bottom in the spectral region of 100-1800 cm^{-1} (a), 2200-3400 cm^{-1} (b).

3.3.5 Discussion

Our Raman measurements of NH_3BH_3 on compression at 180 K as well as the pressure dependence of the characteristic Raman modes collectively suggest three pressure-induced phase transitions at 1.5 GPa, 5 GPa, 8 GPa at 180 K. We note that these transition boundaries are very well aligned with those observed at room temperature by our previous study,[24] i.e., at about 2 GPa, 5 GPa, 8 GPa and 10 GPa. However, the starting structure in each compression sequence is very different, i.e., disordered tetragonal structure (*I*4*mm*) at room temperature versus ordered orthorhombic structure (*Pmn*2_1) at 180 K. It is therefore of interest to understand the possible structures of the high-pressure phases at 180 K and their correlation with those at room temperature. This information, together with previously established room-temperature crystal structures will allow us to extend the phase diagram of NH_3BH_3 to temperatures down to 80 K and pressures up to 15 GPa.

Based on the similar Raman profiles of NH_3BH_3 in the pressure region < 2 GPa at 180 K, it is reasonable to assign the structure in this pressure region (0-1.5 GPa) at 180 K with space group *Pmn*2_1, an extension of the ambient pressure structure below 225 K.[19] The significantly different lattice profile as well as different degrees of splitting of the Raman internal modes of NH_3BH_3 in the subsequent higher pressure regions, however, suggests that the crystal structures of those phases are significantly different than *Pmn*2_1. So far, the known high pressure phases (i.e., > 1.5 GPa) at room temperature have another orthorhombic crystal lattice with space group *Cmc*2_1. Assuming the low-temperature (< 225 K) and high pressure (> 2 GPa) phases have a similar orthorhombic structure, such as *Cmc*2_1, the factor group analysis may help to justify the possible crystal structures as shown in Table II. Starting with molecular symmetry of C_{3v} with irreducible representation shown in Eqn (1), by correlation with factor group C_{2v}^{12} (for *Cmc*2_1) with Z=4 (and thus Z′=2) via Wyckoff site of *C*s symmetry, the irreducible representations of the internal modes and lattice modes of NH_3BH_3 that are Raman active, are:

$$\Gamma_{\text{internal}}^{\text{Cmc2}_1} = 11A_1 + 6A_2 + 6B_1 + 11B_2 \qquad (3)$$

$$\Gamma_{\text{lattice}}^{\text{Cmc2}_1} = 2A_1 + 3A_2 + 2B_1 + 2B_2 \quad (4)$$

Apparently, the maximum number of observed lattice modes (e.g., three) is only a subset of the total of nine predicted Raman active lattice modes under space group *Cmc*2$_1$. In addition, each of the v_1 to v_5 modes individually is predicted to exhibit a doublet whereas modes v_7 to v_{12} should have a quartet Raman profile under the assumed factor group. As a matter of fact, in each pressure region of 1.5-5 GPa, 5-8 GPa and > 8 GPa, the maximum number of observed Raman modes splitting is also less than those predicted except for the v_{11} mode, which matches the prediction exactly (Table 3.2). Incomplete factor group splitting is very common and has been observed in Hess's low-temperature study of NH_3BH_3[19] as well as in other borohydride or amide materials.[20-21] Although there is no contradiction between the observed Raman profiles and the assumed factor group, other similar space groups cannot be ruled out. Detailed *in situ* low-temperature and high-pressure X-ray diffraction measurements will help to elucidate the crystal structures of these phases.

An associated question is what is the nature of the phase transitions at 5 and 8 GPa and the relationship among these higher pressure phases. Vibrational spectroscopy provides sensitive information about molecular structure, nature of bonding, as well as inter-molecular and intra-molecular interactions. As a result, the reduction of intra- and/or inter-molecular distances by compression may significantly enhance these interactions as evidenced by Raman frequency shift, intensity variation, as well as factor group splittings, even within the same or slightly modified crystal lattice. Therefore, phase transitions identified by spectroscopy may not correlate to the X-ray measurements exactly.

Table 3.2 Factor Group Analysis of Vibrational Modes of NH_3BH_3 under Space Group *Cmc*2$_1$

Point group C_{3v}[a]	Site symmetry Cs	Factor group C_{2v}	Raman mode	Counts Predicted	Counts Observed[b]
2×5A_1 →	10A'	5A_1	ν_1	2	1
			ν_2	2	1
			ν_3	2	–[c]
		5B_2	ν_4	2	1
			ν_5	2	1
2×6E →	12A'	6A_1	ν_7	4	2
			ν_8	4	3
		6B_2	ν_9	4	2
	12A"	6A_2	ν_{10}	4	3
			ν_{11}	4	4
		6B_1	ν_{12}	4	2

a. The A_2 mode in C_{3v} symmetry is not Raman active.

b. The maximum number of component for each Raman mode (associated with the original C_{3v} molecular symmetry) in the pressure regions of > 2 GPa.

c. The NH_3 deformation mode ν_3 (1377 cm^{-1}) was not monitored due to the intense Raman mode of diamond.

For instance, although both Lin's and our previous spectroscopic studies suggested multiple phases of NH_3BH_3 at high pressures and room temperature,[24,27] later X-ray measurements and theoretical studies suggest only one major phase transition involving the change of crystal structures from *I*4*mm* to *Cmc*2$_1$.[28-29] Thus it is reasonable to believe that the phase transitions observed in the current low-temperature study may have similar origins as those observed at room-temperature, and therefore, the stability regions of the previously observed high-pressure phases can be extended from room temperature to 80 K. Indeed, for example, the extremely similar Raman profile in this study (e.g., at 8.83 GPa and 180 K from Fig. 3.3) to that from our previous room-temperature study (e.g., at 8.5 GPa from Fig. 3.2) strongly support this understanding. Moreover, the molecular dynamics simulations by Wang et al.[31] suggest that $Cmc2_1$ phase can be obtained from the $Pmn2_1$ structure at high pressure and low temperature, strongly supporting our proposal.

By combining the data of multiple runs following different P-T paths, we can draw a schematic phase diagram roughly outlining the P-T regions of the three known structures: $I4mm$, $Pmn2_1$ and $Cmc2_1$, as shown in Fig. 3.6. We note that although Chen's measurements[29] (open squares) suggested a simple negative T/P slope for the boundary between $I4mm$ and $Cmc2_1$, our measurements show that the slope is almost independent of temperature below 220 K. Furthermore, from the recent combined X-ray, neutron and DFT studies of NH_3BH_3 at room temperature by Kumar et al.,[30] a monoclinic structure with space group $P1$ was proposed above 8 GPa, in excellent agreement with a phase boundary claimed in the current study. However, the lack of significant changes in the Raman patterns across this pressure point, especially that no further splittings of the Raman modes is seen, do not seem to corroborate a crystal structure with such a low symmetry and so many molecular units per primitive cell (i.e., Z=16). We thus labeled this proposed structure in the phase diagram only tentatively. Nonetheless, the band broadening for all Raman modes with the depletion of major modes above 15 GPa and

180 K suggests the transformation to an amorphous phase via significant structural disordering, consistent with the X-ray measurements at room temperature by Chen et al.[29] Again, more detailed *in situ* experiments as well as *ab initio* calculations may help with the understanding of these observations.

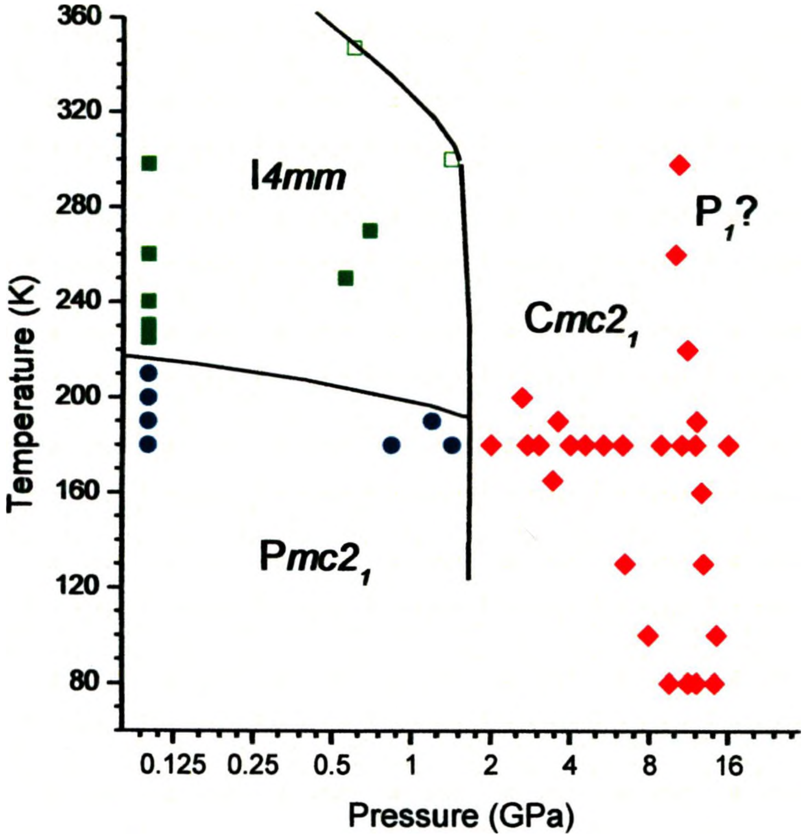

Fig. 3.6 Schematic P-T phase diagram of NH_3BH_3 in the pressure region of 0-15 GPa (in log 2 scale) and temperature region of 80-350 K. Solid symbols are experimental data from the current study, with squares for *I4mm* phase, circles for *Pmc*2_1 phase and diamonds for *Cmc*2_1 phase. The open squares are adopted from Chen's X-ray work (Ref). The solid lines denote the rough boundaries among the three known phases. The P1 phase labeled is considered tentative (see text).

3.4 Conclusions

By *in situ* Raman spectroscopy, we investigated the pressure-temperature induced structural transformations of NH_3BH_3 at pressures up to 15 GPa and temperatures down to 80 K. Upon isothermal compression at 180 K, NH_3BH_3 was found to undergo phase transitions at about 1.5 GPa, 5 GPa and 8 GPa, in excellent alignment with those transitions observed at room temperature in our previous work. In addition, the evolution of Raman spectra with pressure across these transition boundaries, as well as the pressure-dependence of major Raman modes follow a similar pattern to those observed at room temperature. Using factor group analysis, we found the phases above 1.5 GPa are consistent with a crystal structure with space group $Cmc2_1$, although other possibilities cannot be ruled out. The transitions at 5 and 8 GPa can be interpreted as enhanced inter-molecular interactions within the same or possibly slightly modified crystal lattice. Further compression above 15 GPa leads to a gradual transformation to an amorphous phase. Upon decompression and warming up, these P-T induced phase transitions were found to be reversible. Raman data from additional runs following different P-T paths allowed the construction of the P-T phase diagram of NH_3BH_3 where the stability regions of the three previously established structures can be outlined. Further experimental and theoretical investigations are required to justify these understandings.

3.5 Acknowledgements

The authors acknowledge funding support from a Discovery Grant, a Research Tools and Instruments Grant from the Natural Science and Engineering Research Council of Canada, a Leaders Opportunities Fund from the Canadian Foundation for Innovation, an Early Research Award from the Ontario Ministry of Research and Innovation, and a Petro-Canada Young Innovator Award from the University of Western Ontario.

3.6 References

(1) Hamilton, C. W.; Baker, R. T.; Staubitz, A.; Manners, I. *Chem. Soc. Rev.* **2009**, *38*, 279.

(2) Staubitz, A.; Robertson, A. P. M.; Manners, I. *Chem. Rev.* **2010**, *110*, 4079.

(3) Stephens, F. H.; Pons, V.; Baker, R. T. *Dalton T.* **2007**, 2613.

(4) Yang, J.; Sudik, A.; Wolverton, C.; Siegel, D. J. *Chem. Soc. Rev.* **2010**, *39*, 656.

(5) Satyapal, S.; Petrovic, J.; Read, C.; Thomas, G.; Ordaz, G. *Catal. Today* **2007**, *120*, 246.

(6) Chellappa, R. S.; Autrey, T.; Somayazulu, M.; Struzhkin, V. V.; Hemley, R. J. *ChemPhysChem* **2010**, *11*, 93.

(7) Li, Z. Y.; Zhu, G. S.; Lu, G. Q.; Qiu, S. L.; Yao, X. D. *J. Am. Chem. Soc.* **2010**, *132*, 1490.

(8) Osborn, W.; Sadowski, T.; Shaw, L. L. *Scripta Mater.* **2011**, *64*, 737.

(9) Zhang, Y.; Shimoda, K.; Ichikawa, T.; Kojima, Y. *J. Phys. Chem. C* **2010**, *114*, 14662.

(10) Xiong, Z. T.; Yong, C. K.; Wu, G. T.; Chen, P.; Shaw, W.; Karkamkar, A.;

Autrey, T.; Jones, M. O.; Johnson, S. R.; Edwards, P. P.; David, W. I. F. *Nat. Mater.* **2008**, *7*, 138.

(11) Allis, D. G.; Kosmowski, M. E.; Hudson, B. S. *J. Am. Chem. Soc.* **2004**, *126*, 7756.

(12) Cho, H.; Shaw, W. J.; Parvanov, V.; Schenter, G. K.; Karkamkar, A.; Hess, N. J.; Mundy, C.; Kathmann, S.; Sears, J.; Lipton, A. S.; Ellis, P. D.; Autrey, S. T. *J. Phys. Chem. A* **2008**, *112*, 4277.

(13) Dillen, J.; Verhoeven, P. *J. Phys. Chem. A* **2003**, *107*, 2570.

(14) Dixon, D. A.; Gutowski, M. *J. Phys. Chem. A* **2005**, *109*, 5129.

(15) Kathmann, S. M.; Parvanov, V.; Schenter, G. K.; Stowe, A. C.; Daemen, L. L.; Hartl, M.; Linehan, J.; Hess, N. J.; Karkamkar, A.; Autrey, T. *J. Chem. Phys.* **2009**, *130*, 024507.

(16) Bowden, M. E.; Gainsford, G. J.; Robinson, W. T. *Aust. J. Chem.* **2007**, *60*, 149.

(17) Hughes, E. W. *J. Am. Chem. Soc.* **1956**, *78*, 502.

(18) Klooster, W. T.; Koetzle, T. F.; Siegbahn, P. E. M.; Richardson, T. B.; Crabtree, R. H. *J. Am. Chem. Soc.* **1999**, *121*, 6337.

(19) Hess, N. J.; Bowden, M. E.; Parvanov, V. M.; Mundy, C.; Kathmann, S. M.; Schenter, G. K.; Autrey, T. *J. Chem. Phys.* **2008**, *128*, 4508.

(20) Liu, A.; Song, Y. *J. Phys. Chem. B* **2011**, *115*, 7.

(21) Liu, A.; Xie, S. T.; Dabiran-Zohoory, S.; Song, Y. *J. Phys. Chem. C* **2010**, *114*, 11635.

(22) Murli, C.; Song, Y. *J. Phys. Chem. B* **2009**, *113*, 13509.

(23) Song, Y.; Murli, C.; Liu, Z. X. *J. Chem. Phys.* **2009**, *131*, 174506.

(24) Xie, S. T.; Song, Y.; Liu, Z. X. *Can. J. Chem.* **2009,** *87,* 1235.

(25) Custelcean, R.; Dreger, Z. A. *J. Phys. Chem. B* **2003,** *107,* 9231.

(26) Trudel, S.; Gilson, D. F. R. *Inorg. Chem.* **2003,** *42,* 2814.

(27) Lin, Y.; Mao, W. L.; Drozd, V.; Chen, J. H.; Daemen, L. L. *J. Chem. Phys.* **2008,** *129,* 234509.

(28) Filinchuk, Y.; Nevidomskyy, A. H.; Chernyshov, D.; Dmitriev, V. *Phys. Rev. B* **2009,** *79,* 214111.

(29) Chen, J. H.; Couvy, H.; Liu, H. Z.; Drozd, V.; Daemen, L. L.; Zhao, Y. S.; Kao, C. C. *Int. J. Hydrogen Energy* **2010,** *35,* 11064.

(30) Kumar, R. S.; Ke, X. Z.; Zhang, J. Z.; Lin, Z. J.; Vogel, S. C.; Hartl, M.; Sinogeikin, S.; Daemen, L.; Cornelius, A. L.; Chen, C. F.; Zhao, Y. S. *Chem. Phys. Lett.* **2010,** *495,* 203.

(31) Wang, L. C.; Bao, K.; Meng, X.; Wang, X. L.; Jiang, T. T.; Cui, T. A.; Liu, B. B.; Zou, G. T. *J. Chem. Phys.* **2011,** *134,* 024517.

(32) Strobel, T. A.; Somayazulu, M.; Hemley, R. J. *Phys. Rev. Lett.* **2009,** *103,* 065701.

(33) Chellappa, R. S.; Somayazulu, M.; Struzhkin, V. V.; Autrey, T.; Hemley, R. J. *J. Chem. Phys.* **2009,** *131,* 224515.

(34) Lin, Y.; Mao, W. L.; Mao, H. K. *P. Natl. Acad. Sci. USA* **2009,** *106,* 8113.

(35) Mao, W. L.; Mao, H. K.; Goncharov, A. F.; Struzhkin, V. V.; Guo, Q. Z.; Hu, J. Z.; Shu, J. F.; Hemley, R. J.; Somayazulu, M.; Zhao, Y. S. *Science* **2002,** *297,* 2247.

(36) Wang, S. B.; Mao, W. L.; Autrey, T. *J. Chem. Phys.* **2009,** *131,* 144508.

(37) Wang, S. B.; Mao, H. K.; Chen, X. J.; Mao, W. L. *P. Natl. Acad. Sci. USA* **2009,**

106, 14763.

(38) Ragan, D. D.; Gustavsen, R.; Schiferl, D. *J. Appl. Phys.* **1992**, *72*, 5539.

(39) Yen, J.; Nicol, M. *J. Appl. Phys.* **1992**, *72*, 5535.

Chapter 4 Summary and Future work

In this thesis, I have studied the effects of high-pressure effects on two hydrogen storage materials, sodium amide ($NaNH_2$) and ammonia borane (NH_3BH_3), by *in situ* vibrational spectroscopy. Our work represents the first *in situ* high-pressure study of sodium amide by Raman and IR spectroscopies and the first *in situ* high-pressure study of ammonia borane by Raman spectroscopy at low temperatures. Several possible pressure-induced phase transitions were discovered for each compound, and the structural stability and reversibility of these phase transitions were also examined. In addition, possible structures for different phases were discussed. Finally, the implications of their potentials in hydrogen storage application were proposed. These systematic studies on $NaNH_2$ and NH_3BH_3 will aid the design and synthesis of new hydrogen storage materials.

Although this study has provided substantial new spectroscopic and structural information of $NaNH_2$ and NH_3BH_3 under high pressure, more detailed work still need to be done. For example, the proposed structures in each phase need to be confirmed by X-ray or neutron diffraction and compared with the spectroscopic results. And high-pressure measurements on ammonia borane at low temperatures could supplement to our low-temperature Raman results.

In addition, both $NaNH_2$ and NH_3BH_3 are known to release H_2 via pyrolysis. Therefore, the investigation of Raman and IR spectra as a function of temperature combined with pressure will greatly enhance our understanding of temperature-pressure-induced structural transformations and H_2 release that $NaNH_2$ and NH_3BH_3 may undergo. Furthermore, by reacting with H_2 under high pressure, NH_3BH_3 has been found to form a new hydrogen storage complex, i.e., NH_3BH_3-H_2 which can store ~ 8-12 wt % more hydrogen than NH_3BH_3.[1-5] Therefore, the synthesis of hydrogen storage materials similar to the NH_3BH_3-H_2 system at high pressures should be explored in other systems, such as $NaNH_2$-H_2. Finally, high pressure studies on other kinds of hydrides could provide more choices for hydrogen storage materials and more in-depth understanding of the properties and mechanism under high pressures.

References

(1) Liu, A.; Song, Y. *J. Phys. Chem. C* **2011,** *submitted.*

(2) Lin, Y.; Mao, W. L.; Mao, H. K. *P. Natl. Acad. Sci. USA* **2009**, *106*, 8113.

(3) Yang, J. B.; Lamsal, J.; Cai, Q.; James, W. J.; Yelon, W. B. *Appl. Phys. Lett.* **2008,** *92*, 9.

(4) Stephens, F. H.; Pons, V.; Baker, R. T. *Dalton T.* **2007**, 2613.

(5) Trudel, S.; Gilson, D. F. R. *Inorg. Chem.* **2003**, *42*, 2814.

Appendix :NaNH$_2$ X-ray diffraction patterns

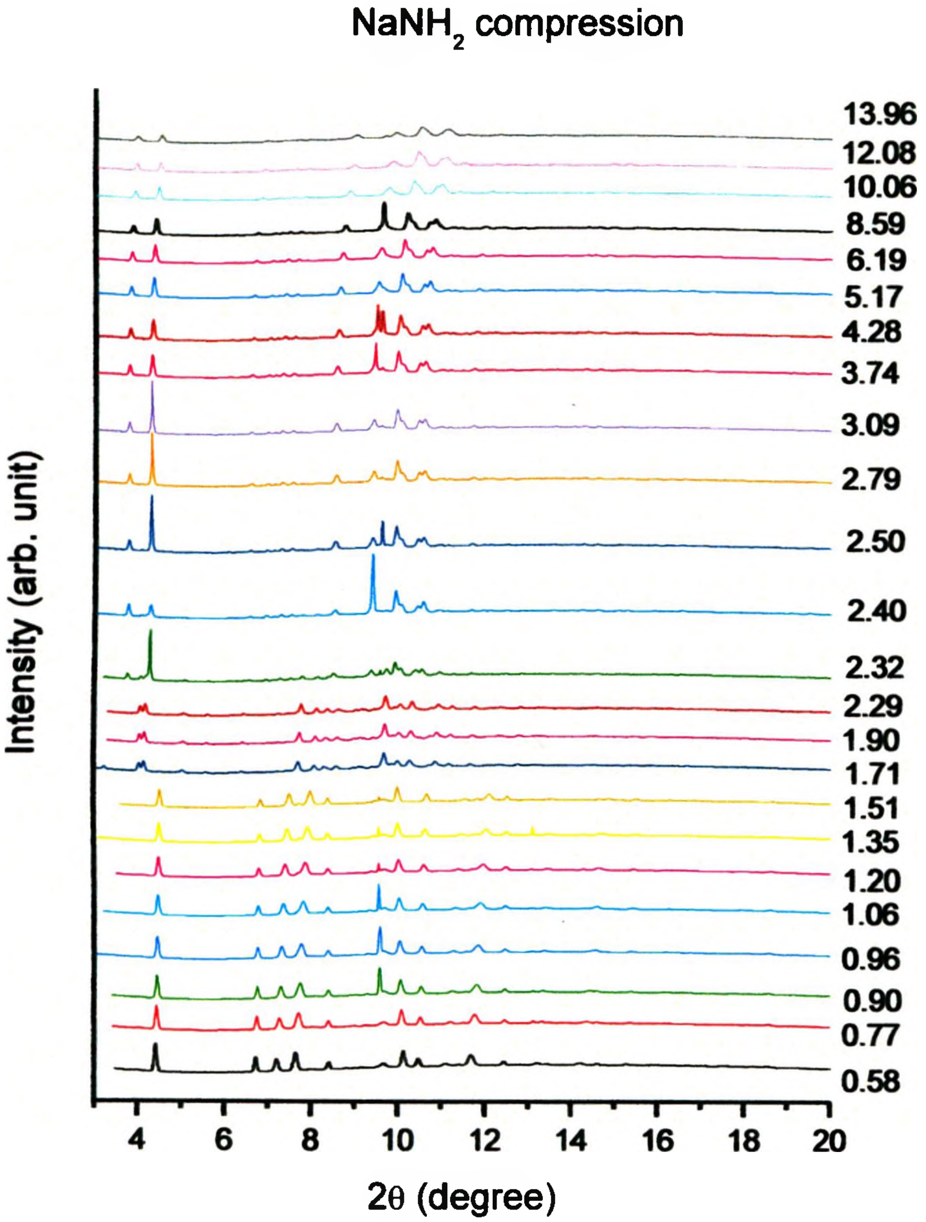

Fig. A1 1D X-ray diffraction patterns of NaNH$_2$ on compression. The pressure in GPa are labeled for each spectrum. The patterns are offset for clarity.

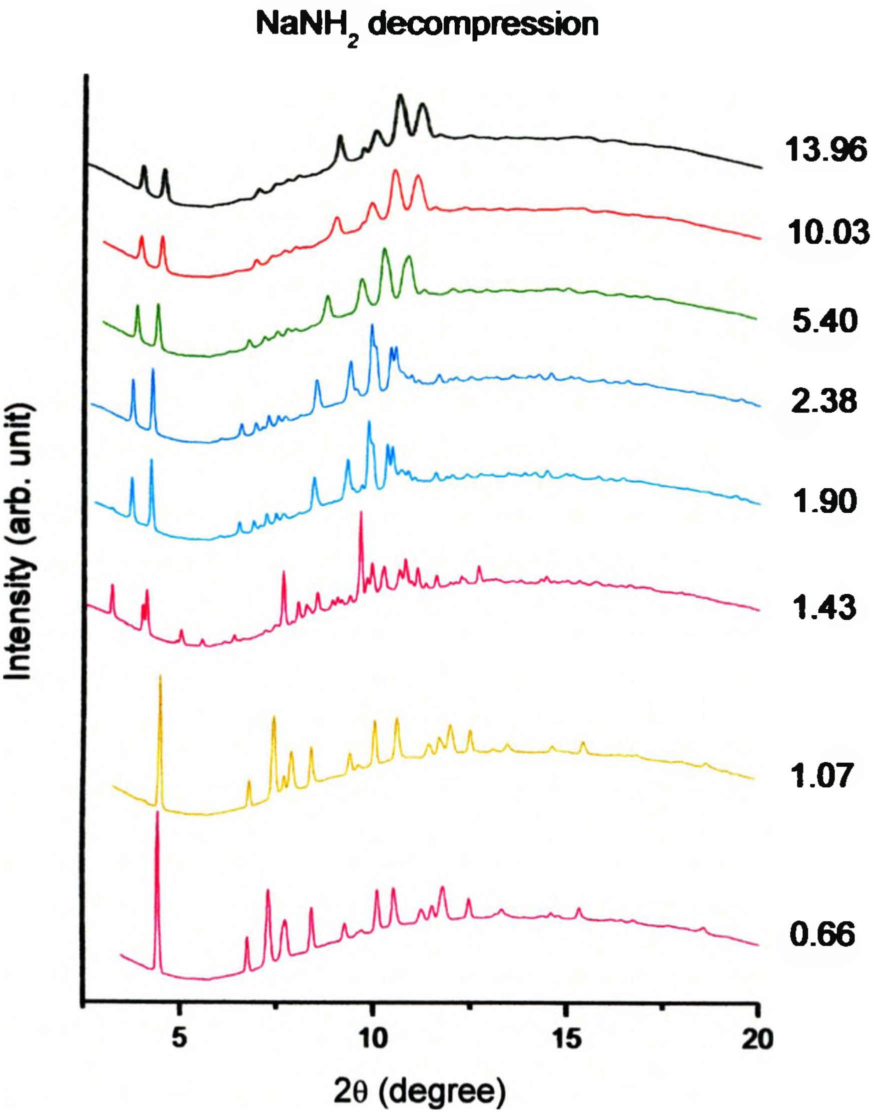

Fig. A2 1D X-ray diffraction patterns of $NaNH_2$ on decompression. The pressure in GPa are labeled for each spectrum. The patterns are offset for clarity.

Copyrighted Material and Permissions

Copyright permission for published and submitted material from theses and dissertations http://pubs.acs.org/userimages/ContentEditor/1218205107465/dissertation.pdf

ACS extends blanket permission to students to include in their theses and dissertations their own articles, or portions thereof, that have been published in ACS journals or submitted to ACS journals for publication, provided that the ACS copyright credit line is noted on the appropriate page(s).

Permission for this particular request is granted for print and electronic formats at no charge. Figures and tables may be modified. Appropriate credit should be given. Please print this page for your records and provide a copy to your publisher. Requests for up to 4 figures require only this record. Five or more figures will generate a printout of additional terms and conditions.

Chapter 2

Appropriate credit should read: "Reprinted with permission from {Liu, A. & Song, Y. In Situ High-Pressure Study of Sodium Amide by Raman and Infrared Spectroscopies. *J Phys Chem B* **115**, 7-13}. Copyright {2011} American Chemical Society."

Website: http://pubs.acs.org/doi/abs/10.1021/jp107285r

Chapter 3

Reproduced with permission from [The Journal of Physical Chemistry C] (Title: “In situ High-Pressure and Low-Temperature Study of Ammonia Borane by Raman Spectroscopy”; Author(s): Liu, Ang; Song, Yang), submitted for publication. Unpublished work copyright [2011] American Chemical Society